



UNIVERSITY OF LEEDS

This is a repository copy of *Morphological population balance modelling of the effect of crystallisation environment on the evolution of crystal size and shape of para-aminobenzoic acid*.

White Rose Research Online URL for this paper:
<http://eprints.whiterose.ac.uk/146316/>

Version: Accepted Version

Article:

Ma, CY orcid.org/0000-0002-4576-7411 and Roberts, KJ orcid.org/0000-0002-1070-7435
(2019) Morphological population balance modelling of the effect of crystallisation environment on the evolution of crystal size and shape of para-aminobenzoic acid. *Computers & Chemical Engineering*, 126. pp. 356-370. ISSN 0098-1354

<https://doi.org/10.1016/j.compchemeng.2019.04.019>

© 2019 Elsevier Ltd. All rights reserved. This manuscript version is made available under the CC-BY-NC-ND 4.0 license <http://creativecommons.org/licenses/by-nc-nd/4.0/>.

Reuse

This article is distributed under the terms of the Creative Commons Attribution-NonCommercial-NoDerivs (CC BY-NC-ND) licence. This licence only allows you to download this work and share it with others as long as you credit the authors, but you can't change the article in any way or use it commercially. More information and the full terms of the licence here: <https://creativecommons.org/licenses/>

Takedown

If you consider content in White Rose Research Online to be in breach of UK law, please notify us by emailing eprints@whiterose.ac.uk including the URL of the record and the reason for the withdrawal request.



eprints@whiterose.ac.uk
<https://eprints.whiterose.ac.uk/>

29 **Abstract**

30 A current morphological population balance (MPB) modelling methodology, which integrates crystal
31 morphology, facet growth kinetics with multi-dimensional population balance, is overviewed and
32 demonstrated, hence providing an attractive approach for modelling crystallisation processes. MPB
33 modelling is applied to simulate the batch crystallisation of the alpha-form of para-aminobenzoic acid
34 from ethanolic solutions as a function of the crystallisation environment including cooling rate,
35 seeding temperature and seed conditions (loading, size and shape). The evolution of crystal shape/size
36 and their distributions revealed that higher loading led to smaller and less needle-like crystals with
37 similar yields, hence potentially being an important parameter for process control. Examination of
38 the development of the fracture surface for broken seeds, mimicking the seed conditions after milling
39 in practice in the simulated processes, demonstrated that these faces grew fast and then rapidly
40 disappeared from the external crystal morphology. Restriction and challenges inherent in the current
41 model are also highlighted.

42

43 **Keywords:** Morphological Population Balance, Crystal Shape Distribution, Crystal Size
44 Distribution, Crystallisation, Para-aminobenzoic Acid, Crystallisation Environment

45

46 **1. Introduction**

47 Recent reviews (Bell, 2017, Maier, 2017) have highlighted that the development of new technologies
48 has the potential to deliver a step-change in the way we make medicines through the adoption of state-
49 of-the-art simulation-based tools. Through this, more ‘near patient’ medicines (combination
50 medicines, wider range of dosage forms, stratified formulation) can be delivered through the much
51 greater agility provided by digital design and automation. Digital design potentially provides the route
52 to the preparation of the solution re-crystallised pharmaceuticals which have e.g. low structural
53 variability, high purity and narrow size/shape distribution with concomitantly enhanced product
54 properties. Such materials could have significant patient benefits such as narrow therapeutic profiles,
55 higher stability and longer shelf life, greater content uniformity, etc. and as such represent a critical
56 objective for the delivery of medicines with pre-defined properties for industry and society. Active
57 pharmaceutical ingredient (API) and excipients used in their formulation often have well-defined
58 crystal morphologies and hence surface chemistry, and thus their physical properties can be defined
59 and manipulated through modelling, optimisation and control of crystallisation processes. Such
60 surface properties can provide the key parameters for delivering both drug product quality (such as
61 high purity and lack of variability) and performance (such as bioavailability and stability), and also
62 ensuring the same particles encompassed within the API are present in the formulated drug product
63 and are also transferred from R&D into manufacturing stage.

64 Most drugs are still manufactured in the traditional way, i.e. through processes designed to deliver
65 tasks such as crystallisation for enabling product purity, form and yield. However, each of these
66 discrete steps is not necessarily considering and/or directly linking with their resultant effect of the
67 resultant crystal properties on the downstream processes. Therefore, a crystallisation process
68 generally produces crystals with dispersion of size/shape. However, for the growing area of targeted
69 medicines, such variations create challenges as they have mindful of their potentials to affect the drug
70 crystal’s dissolution and hence its efficacy, i.e. crystals with different sizes/shapes create variability
71 in the in-vitro dissolution. Currently, to achieve the required size/shape and their distributions for
72 drug formulation, crystal particles are milled to effect the size reduction needed. However, such
73 intensive mechanical processing can impact on the crystal’s surface properties through the creation
74 of new high surface energy, fracture surfaces and lattice defects such as dislocations, as well as
75 significantly enhancing surface roughness and hence area. In extreme cases, milling can cause
76 polymorphic form transformation. Similarly, blending/granulation for mixing with binder/excipients
77 to produce granules may need to be broken into smaller size for compaction/tableting processes. In
78 principle, crystals and excipients could be produced with a much tighter specification such that they
79 could be directly compressed and tableted into the final product without the need for milling and

80 granulation processes, and also avoiding variability due to changes in, and/or damage to, crystal
81 surface properties. In pharmaceutical product development, crystallisation processes are widely used
82 but many ingredients exhibit needle-like, plate-like or rod-like crystal morphologies, which can
83 directly affect their downstream particle processing properties such as filterability, flowability,
84 tabletability. Therefore, digital design of crystallisation processes based on first-principles physical
85 chemical models can become an important bottleneck to breakthrough.

86 Traditional population balance (PB) models use a length (or radius of a volume equivalent sphere)
87 for one-dimensional characteristic size or length and width for two-dimensional characteristic sizes
88 with a shape factor for calculating crystal volume. Assuming the crystal morphology does not change
89 during crystallisation processes, the evolution of crystal shape/size could be represented (e.g.,
90 (Lovette et al., 2008, Zhang and Doherty, 2004, Kuvadia and Doherty, 2013)). Morphological PB
91 (MPB) (e.g. (Ma et al., 2008)) was developed to remove the assumption that crystal morphology is
92 invariant during crystallisation, through directly integrating both base crystal morphology and face-
93 specific growth kinetics with the PB model, hence capturing the change of crystal shape/size and
94 through their face {hkl}-specific properties. A more detailed review of previous work is given in
95 Supplementary materials (S1).

96 In this paper, the MPB method is overviewed and demonstrated through a numerical study of a
97 pharmaceutical compound, α -pABA, crystallised from ethanolic solution. In this, the face-specific
98 growth mechanisms and rate equations were obtained by fitting the experimental data as obtained
99 from the literature (Toroz et al., 2015). The performance of crystallisation processes is examined
100 using MPB modelling to predict the evolution of crystal shape/size distributions in a seeded batch
101 cooling crystalliser under different cooling rate, seeding and seed conditions including assessing the
102 impact of broken seeds on the properties of the final products.

103

104 **2. Morphological Population Balance for Crystallisation Process Design**

105 **2.1 MPB Modelling Framework**

106 The framework for prediction of the distributions of crystals size and shape for crystallisation
107 processes using MPB modelling is schematically shown in Figure 1. For the known crystal shape and
108 size, the centre of the crystal and the corresponding normal distances from individual faces, which
109 can be defined by the Miller Index {hkl} (a notion system in crystallography for crystal planes/faces)
110 such as $\{h_1k_1l_1\}$, $\{h_2k_2l_2\}$ and $\{h_3k_3l_3\}$ in Figure 1, to the centre can be determined with individual
111 variables such as x_1 , x_2 and x_3 in Figure 1. During crystallisation processes, these variables are under
112 continuous evolution as the processes are controlled by various crystallisation mechanisms including

113 nucleation, growth, agglomeration, breakage and crystallisation environment. Therefore these
114 variables can be treated as the independent variables for the formulation of MPB equation. As shown
115 in Figure 1, nucleation, face-specific growth kinetics, face-based agglomeration and breakage kernels
116 are the key input parameters for MPB modelling, which can be determined through various modelling
117 and experimental studies. The solution of the MPB equation will generate the evolution of these
118 independent variables, i.e. normal distances, of all crystals, hence their distributions at each
119 crystallisation time. Based on the known crystal morphology, each combination of normal distances
120 (x_1, x_2, x_3) represents a crystal shape with the distribution providing the number of crystals having
121 this shape. Therefore, after the crystal size/shape analysis, a crystal shape distribution can be formed
122 and examined to see whether the distribution meets the requirements for precision particles. If not
123 (Figure 1), the MPB can optimise and control the crystallisation environment, hence achieving the
124 required crystal shape distribution.

125

126

127

128

129

130

131

132

133

134

135

136

137

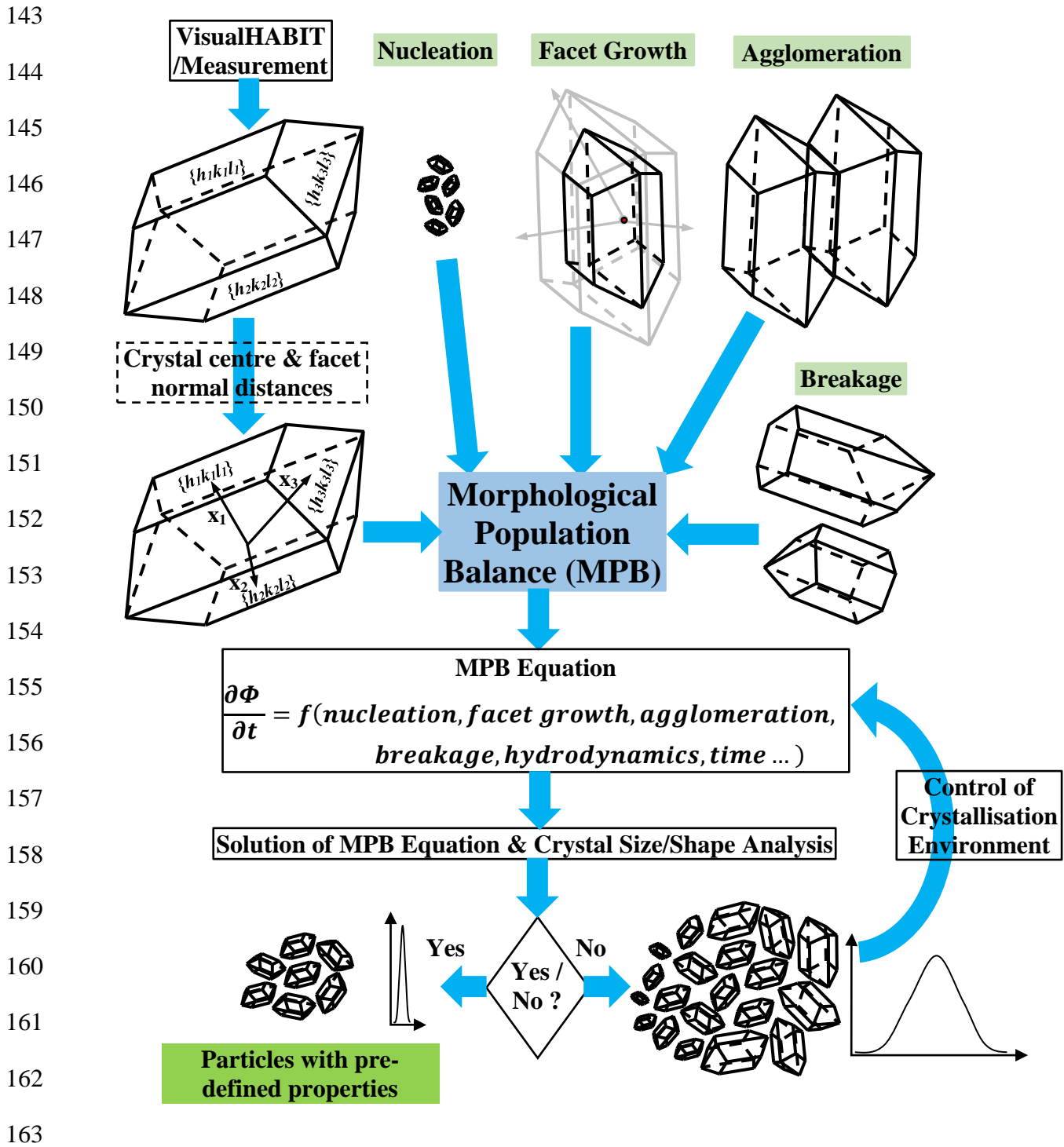
138

139

140

141

142



164 **Figure 1.** Schematic of a framework for digital design of crystals with pre-defined size/shape and
 165 their distributions using MPB modelling. Note that $\{h_1k_1l_1\}$, $\{h_2k_2l_2\}$ and $\{h_3k_3l_3\}$ are the Miller
 166 Indices of the crystal and x_1 , x_2 and x_3 are the corresponding normal distances from the individual
 167 faces to the centre of the crystal, Φ and t are the number population density function of crystals and
 168 crystallisation processing time, respectively.

169

170

171 2.2 MPB Model Formulation

172 The general PB model formulation to describe particulate systems with internal and external variables
173 can be found in literature (e.g., (Hulburt and Katz, 1964, Ramkrishna and Mahoney, 2002, Randolph
174 and Larson, 1988)). In this study, the MPB methodology identifies and defines the normal distances
175 from faces ($\{h_1k_1l_1\}$, $\{h_2k_2l_2\}$ and $\{h_3k_3l_3\}$) to the crystal centre as three independent dimension
176 variables (x_1 , x_2 , x_3), respectively, as shown in Figure 1. The PB equation for seeded batch cooling
177 crystallisation processes in a well-mixed batch crystalliser without nucleation, agglomeration and
178 breakage to simplify the case study of MPB for pharmaceutical crystallisation can be written as (e.g.,
179 (Ma and Roberts, 2018, Ma et al., 2008, Marchal et al., 1988, Puel et al., 2003)):

$$\begin{aligned} 180 & \frac{1}{V_T(t)} \frac{\partial}{\partial t} [\Phi(x_1, x_2, x_3, t) V_T(t)] + \frac{\partial}{\partial x_1} [\Phi(x_1, x_2, x_3, t) G_1(x_1, t)] + \frac{\partial}{\partial x_2} [\Phi(x_1, x_2, x_3, t) G_2(x_2, t)] + \\ 181 & \frac{\partial}{\partial x_3} [\Phi(x_1, x_2, x_3, t) G_3(x_3, t)] = 0 \end{aligned} \quad (1)$$

182 where V_T is the total volume of solution (or slurry after seeding) in a crystalliser; t is the processing
183 time; Φ is the number population density function of crystals; G_i ($i = 1, 3$) is the growth rate in the x_i
184 ($i = 1, 3$) direction. The corresponding initial condition is the size/shape distribution as a function of
185 the three variables (x_1 , x_2 , x_3) at the time of zero, i.e., $\Phi(x_1, x_2, x_3, t)|_{t=0} = 0$. For a batch cooling
186 crystallisation process, the boundary conditions for Eq. (1) are $\Phi(x_{1,i}, x_{2,j}, x_{3,k}, t)|_{i=1 \text{ or } N_1} = 0$ ($j =$
187 $1, N_2$; $k = 1, N_3$), $\Phi(x_{1,i}, x_{2,j}, x_{3,k}, t)|_{j=1 \text{ or } N_2} = 0$ ($i = 1, N_1$; $k = 1, N_3$) and
188 $\Phi(x_{1,i}, x_{2,j}, x_{3,k}, t)|_{k=1 \text{ or } N_3} = 0$ ($i = 1, N_1$; $j = 1, N_2$), where N_1 , N_2 , N_3 are the total number of
189 classes for the (x_1 , x_2 , x_3) size domains (see the Supplementary materials (S3) for the definitions of
190 other parameters). It is worth to note that three dimensions (x_1 , x_2 , x_3) are not Cartesian coordinates,
191 hence they are not perpendicular to each other. Furthermore, depending on the number of independent
192 crystal faces identified, the MPB techniques can generate the MPB equation with the corresponding
193 number of dimensions. The growth rates of individual faces such as ($\{h_1k_1l_1\}$, $\{h_2k_2l_2\}$ and $\{h_3k_3l_3\}$)
194 can be obtained through fitting with measured crystal growth data (see more detail in the
195 Supplementary materials (S2)). The discretisation method can be used to form multi-dimensional
196 ordinary differential equations for their solution with a standard solver such as the Runge-Kutta-
197 Fehlbergh solver (see further details in the Supplementary materials (S3) and Section 3.2).

198

199

200

201

202 3. MPB Modelling of α -pABA Crystallised from Ethanolic Solutions

203 3.1 Materials and Solute-Solvent System

204 The organic compound, para aminobenzoic acid, provides an important representative compound for
205 fundamental study (Rosbottom et al., 2017, Rosbottom, 2016, Toroz et al., 2015, Rosbottom et al.,
206 2015, Sullivan et al., 2014, Nguyen et al., 2014). The α polymorphic form, α -pABA, can be readily
207 crystallised from ethanol solvent in a 0.5L batch crystalliser using a seeded cooling process. The
208 pABA molecular structure shows that it consists of a phenyl ring with a carboxylic acid group and an
209 amino group in the para position (Rosbottom et al., 2015). Through crystallographic studies and
210 molecular modelling, the α -pABA crystal morphology (Figure 2) can be characterised by 8 stable
211 crystal faces (2 {101}, 2 {10-1} and 4 {011} faces) in a monoclinic crystal structure with the space
212 group $P2_1/n$ (Rosbottom et al., 2015). The α -pABA crystal structure comprises two molecules in the
213 asymmetric unit and eight molecules in the unit cell with cell dimensions: $a = 18.55 \text{ \AA}$, $b = 3.86 \text{ \AA}$, c
214 $= 18.64 \text{ \AA}$ and $\beta = 93.56^\circ$ (a , b , c and β are the unit cell parameters) The intermolecular packing
215 arrangement within the structure is dominated by the formation of two non-equivalent $\text{OH}\cdots\text{O}$ H-
216 bonding dimers between neighbouring carboxylic acid groups, and also by $\pi - \pi$ stacking interactions
217 created by the head to head stacking motif of the pABA molecules along the b direction. Overall, the
218 α form of pABA crystal is observed to have a needle-like or lath-like morphology elongated along
219 the b -crystallographic axis which is a typical crystal shape for many pharmaceutical solids. Further
220 detail can be found in literature (Rosbottom et al., 2015, Toroz et al., 2015).

221 Based on the crystal morphology of α -pABA (Figure 2) and the definition of independent variables
222 for MPB modelling in Section 2, the three variables for MPB simulation of α -pABA crystallisation
223 from ethanol can be determined as shown in Figure 2.

224

225

226

227

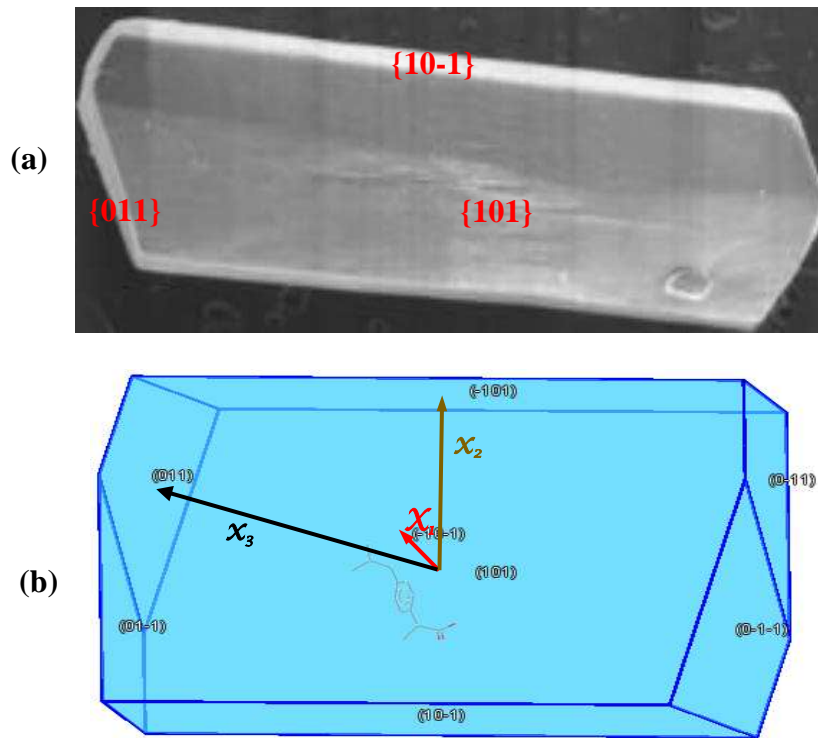
228

229

230

231

232



244 **Figure 2.** The α -pABA crystal shape (single crystal image from (Rosbottom, 2016) and prediction
 245 by VisualHABIT (Clydesdale et al., 1991, Clydesdale et al., 1996, Pickering et al., 2017)) and the
 246 definitions of the three independent dimension variables (x_1 , x_2 , x_3) perpendicular to its three dominant
 247 crystal faces $\{101\}$, $\{10-1\}$, $\{011\}$ for MPB modelling.

248

249 The solubility of α -pABA in ethanol solvent were obtained from literature (Toroz et al., 2015,
 250 Rosbottom et al., 2017) using an isothermal technique. The experiments were carried out at the 1.5
 251 ml scale with 300 rpm micro magnetic-bar stirring using an Avantium Crystal16 unit.

252 The facet crystal growth rates in the x_1 , x_2 and x_3 face directions of α -pABA growing in ethanol were
 253 measured by an optical microscopy in a crystal growth cell (Toroz et al., 2015), with more detail to
 254 be found in (Toroz et al., 2015, Nguyen et al., 2014).

255

256 **3.2 Crystallisation Environment and MPB Solution**

257 The obtained three dimensional MPB equation, together with available solubility and faceted growth
 258 rate equations based on single crystal experimental data from Toroz et al. (Toroz et al., 2015), was
 259 solved with the following operating conditions: cooling rate (CR) of 0.5°C/min, saturation
 260 concentration of 0.222 kg/kg (saturated temperature of 45°C), seeding point of 20.5°C with the
 261 corresponding supersaturation, S , (= solute concentration (C) / solubility) of 1.5, seed loading of 0.1%
 262 (by mass), and seed mean x_1 , x_2 and x_3 of 22, 37 and 58 μm . Using the above operating conditions as

263 a base case (green coloured in Table 1), further simulations were carried out to investigate the effect
 264 of different operating conditions (Table 1) on the crystal size/shape evolution of α -pABA
 265 crystallisation, including different CR of 0.05 – 1.5°C/min, various seeding temperatures (T_{seeds}) of
 266 20.5 – 39.0°C (corresponding to supersaturation at the seeding points (S_{seeds}) of 1.5 – 1.1), different
 267 seed loadings (X_{seeds}) of 0.1 – 5.0%, initial mean size/shape of seeds (M_{seeds} ($\bar{x}_1, \bar{x}_2, \bar{x}_3$) are the mean
 268 sizes of variable (x_1, x_2, x_3) and the corresponding ($\sigma_{x_1}, \sigma_{x_2}, \sigma_{x_3}$) are the standard deviations), and
 269 other special operating conditions such as broken seeds. All of the simulations were terminated when
 270 the supersaturation reached to 1.01, indicating that crystal growth in all face directions became close
 271 to zero, hence any further crystallisation process would not vary the size/shape distributions, yield of
 272 the final products.

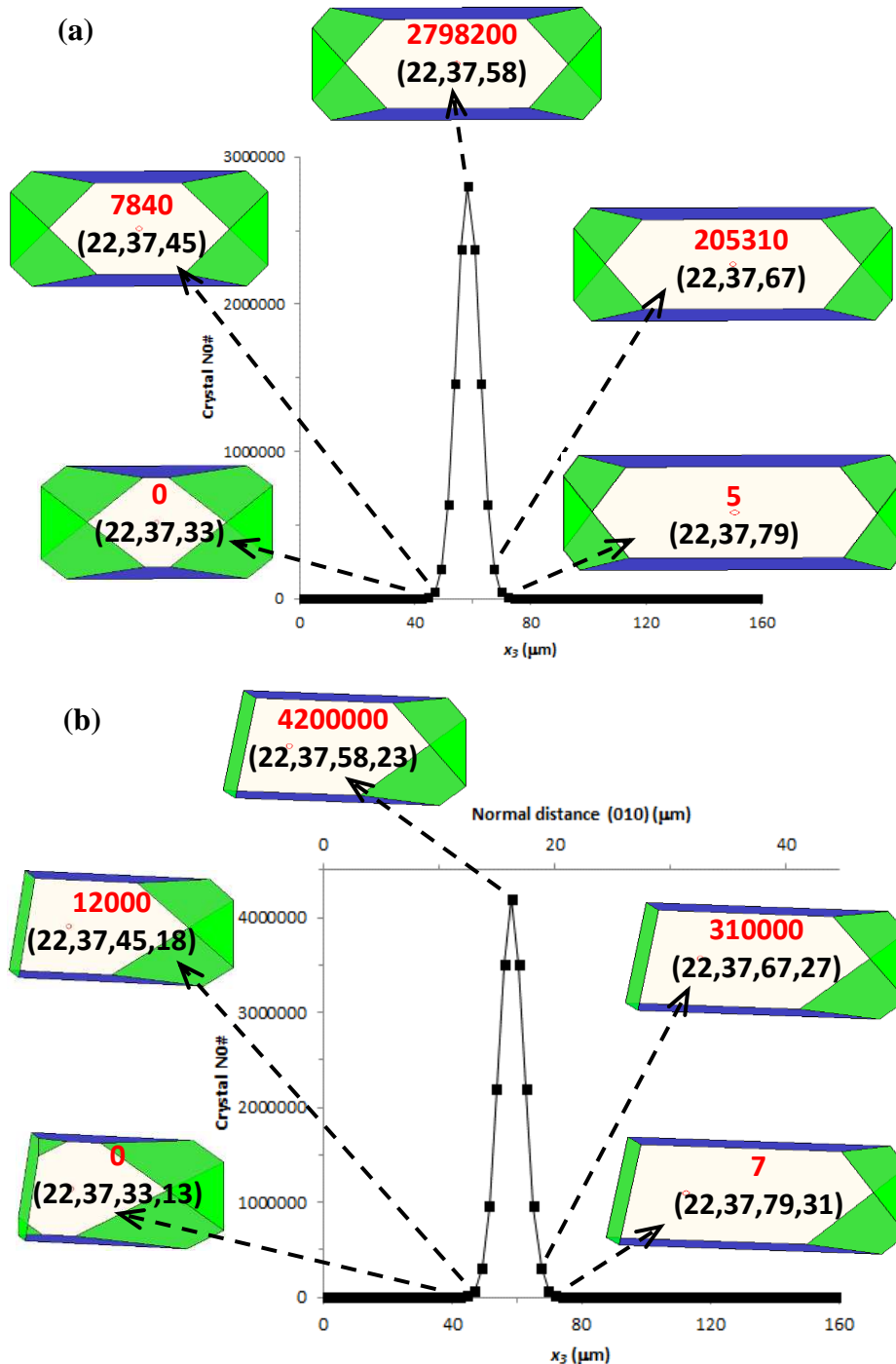
273

274 **Table 1.** Operating conditions used for MPB simulations

Cooling rate (CR)							
CR (°C/min)	Saturation concentration C (kg/kg)	Saturation T (°C)	Seeding point – T_{seeds} (°C)	S_{seeds} (-)	X_{seeds} (% mass)	M_{seeds} ($\bar{x}_1, \bar{x}_2, \bar{x}_3$) (μm)	Seeds standard deviations - ($\sigma_{x_1}, \sigma_{x_2}, \sigma_{x_3}$) (μm)
0.05	0.222	45	20.5	1.5	0.1	22, 37, 58	8, 8, 8
0.5	0.222	45	20.5	1.5	0.1	22, 37, 58	8, 8, 8
1.0	0.222	45	20.5	1.5	0.1	22, 37, 58	8, 8, 8
1.5	0.222	45	20.5	1.5	0.1	22, 37, 58	8, 8, 8
Seeding point (T_{seeds} or S_{seeds})							
0.5	0.222	45	39.0	1.1	0.1	22, 37, 58	8, 8, 8
0.5	0.222	45	33.7	1.2	0.1	22, 37, 58	8, 8, 8
0.5	0.222	45	28.9	1.3	0.1	22, 37, 58	8, 8, 8
0.5	0.222	45	24.7	1.4	0.1	22, 37, 58	8, 8, 8
0.5	0.222	45	20.5	1.5	0.1	22, 37, 58	8, 8, 8
Seed loading (X_{seeds})							
0.5	0.222	45	20.5	1.5	0.1	22, 37, 58	8, 8, 8
0.5	0.222	45	20.5	1.5	0.5	22, 37, 58	8, 8, 8
0.5	0.222	45	20.5	1.5	1.0	22, 37, 58	8, 8, 8
0.5	0.222	45	20.5	1.5	2.0	22, 37, 58	8, 8, 8
0.5	0.222	45	20.5	1.5	5.0	22, 37, 58	8, 8, 8
Seed mean shape (M_{seeds})							
0.5	0.222	45	20.5	1.5	0.1	22, 37, 58	8, 8, 8
0.5	0.222	45	20.5	1.5	0.1	22, 27, 40	8, 8, 8
0.5	0.222	45	20.5	1.5	0.1	22, 27, 131	8, 8, 8

275

276 The typical seeds distributions for perfect and broken crystals are shown in Figure 3. With fixed mean
 277 sizes, M_{seeds} , $(\bar{x}_1, \bar{x}_2, \bar{x}_3)$ of (22, 37, 58 μm) and standard deviations $(\sigma_{x_1}, \sigma_{x_2}, \sigma_{x_3})$ of (8, 8, 8 μm), a
 278 Gaussian distribution of seeds crystals, $\Phi(x_1, x_2, x_3, 0)$, can be obtained using the pre-defined seeds
 279 loading (X_{seeds}). With the same amount of seed loading, the case with broken seeds (Figure 3b) has
 280 higher number of crystals. In Figure 3b, the bottom horizontal axis, z , is based on the face $\{011\}$ at
 281 the side without breakage, i.e. the right side of the crystals, whilst the top horizontal axis is based on
 282 the broken face (010).



304 **Figure 3.** Typical seeds shape/size distributions: (a) perfect seed crystals, (b) broken seed crystals at
 305 the mean normal distances of faces {101} and {10-1}, i.e. x_1 and x_2 . Note that the three values in the
 306 brackets in a) represent the normal distances of faces {101}, {10-1} and {011}, and the first three
 307 values in the brackets in b) represent the normal distances of faces {101}, {10-1} and {011} with the
 308 fourth one for the broken face (010).

309

310 With the MPB equation and discretisation method described in the Section 2.2 and Supplementary
 311 materials (S3), respectively, the (x_1, x_2, x_3) 3D domain of normal distances was discretised into (70,
 312 70, 70) classes over the size ranges of three normal distances. The discretised MPB equations,
 313 together with a Gaussian-type initial distribution of seeds size/shape (as shown in Figure 3), and the
 314 other operating conditions (as listed in Table 1), were solved using the Runge-Kutta-Fehlbergh 4th/5th-
 315 order solver (Shampine and Watts, 1977) with an automatic time-step control to obtain the evolution
 316 of normal distances in three face directions.

317

318 4. Results and Discussion

319 4.1 Solubility and Facet Growth Rates

320 The data obtained from literature (Toroz et al., 2015) were analysed to obtain the following solubility
 321 equation:

$$322 \quad C^* = e^{\left(-\frac{1568}{T} + 2.3333\right)} \quad (2)$$

323 where T is the solution temperature (°C).

324 The experimental data of face-specific experimental data of growth rates of single crystals in a growth
 325 cell was collected by Toroz et al. (Toroz et al., 2015). The corresponding growth cell setup can be
 326 found in Nguyen et al. (Nguyen et al., 2014, Turner et al., 2019). Based on the experimental data
 327 (Toroz et al., 2015) and the face-specific growth kinetics described in the Supplementary materials
 328 (S2), the fit of growth rate in the face direction of {011} as a function of supersaturation was found
 329 to correspond to an RIG mechanism ($r = 1$ in Eq. (S.1)) even at low supersaturations. The
 330 corresponding facet growth rate of face {011}, G_3 , is as follows:

$$331 \quad G_3 = G\{011\} = \frac{S-1.0015}{8.65 \times 10^{-4} + \frac{1}{2.0 \times 10^5 \times (S-1.0015)^0}} \quad (3)$$

332 From Eq. (3), it can be seen that the diffusion related term with a value of 8.65×10^{-4} is over 2 times
 333 magnitude larger than that for the surface integration term (5×10^{-6}). Therefore the rate of crystal

334 growth of face {011} is diffusion limited by diffusion mass transfer (Camacho et al., 2016), i.e. the
 335 crystal growth is controlled by how fast the solute molecules in bulk solution diffuses from the bulk
 336 solution and across the solid/solution boundary layer for integrating with (growing on) the crystal
 337 face. From molecular modelling studies (Rosbottom et al., 2015, Toroz et al., 2015), the $\pi - \pi$
 338 interactions dominate the growth on the {011} faces and the attachment of pABA molecules via the
 339 $\pi - \pi$ stacking motif may lead to a solid-solid integration mechanism at the surface, hence any growth
 340 spirals present at this surface. Therefore the diffusion of molecules to the surface controls the growth
 341 of face {011}, as also indicated by Eq. (3).

342 The fitting of the growth rate in the {10-1} face direction, G_2 , corresponds to a birth and spread (B&S)
 343 growth mechanism (Eq. (S.2)) with the following equation:

$$344 \quad G_2 = G\{10 - 1\} = \frac{S-1.01}{9.54 \times 10^{-3} + \frac{1}{4.0 \times 10^4 \times (S-1.01)^{-1/6} \times \exp\left(\frac{0.5}{S-1.01}\right)}} \quad (4)$$

345 As both the diffusion related term and surface integration term have similar values (see Eq. (4)), the
 346 diffusion (mass transfer) and surface integration have the similar effect on the crystal growth of face
 347 {10-1}.

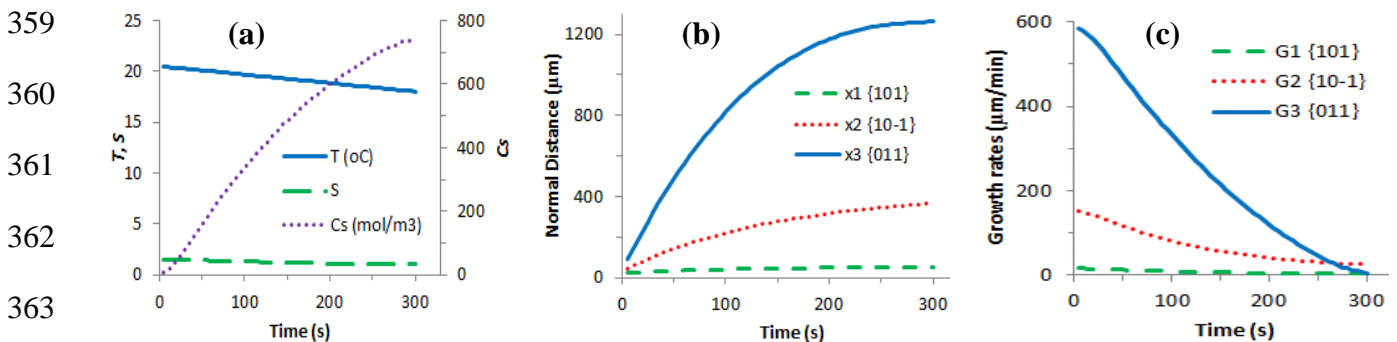
348 It was found that the growth of α -pABA crystals in the {101} face direction was too slow to measure
 349 directly and thus the {101} face growth rate, G_1 , was estimated from G_2 based on the ratio of
 350 attachment energies between face {101} and face {10-1} (Rosbottom et al., 2015). Hence

$$351 \quad G_1 = G\{101\} = 0.1 * G_2 \quad (5)$$

352

353 4.2 Base Case

354 Figure 4 shows the simulated solution temperature, supersaturation, crystal concentration, mean
 355 normal distances (x_1, x_2, x_3) for faces {101}, {10-1}, {011}, and the corresponding facet growth rates
 356 at a cooling rate (CR) of 0.5°C/min. The mean normal distance for face {011} increased rapidly with
 357 time as the face {011} is the fastest growing face from previous studies (Rosbottom et al., 2015,
 358 Toroz et al., 2015), while less growth happened in x direction.

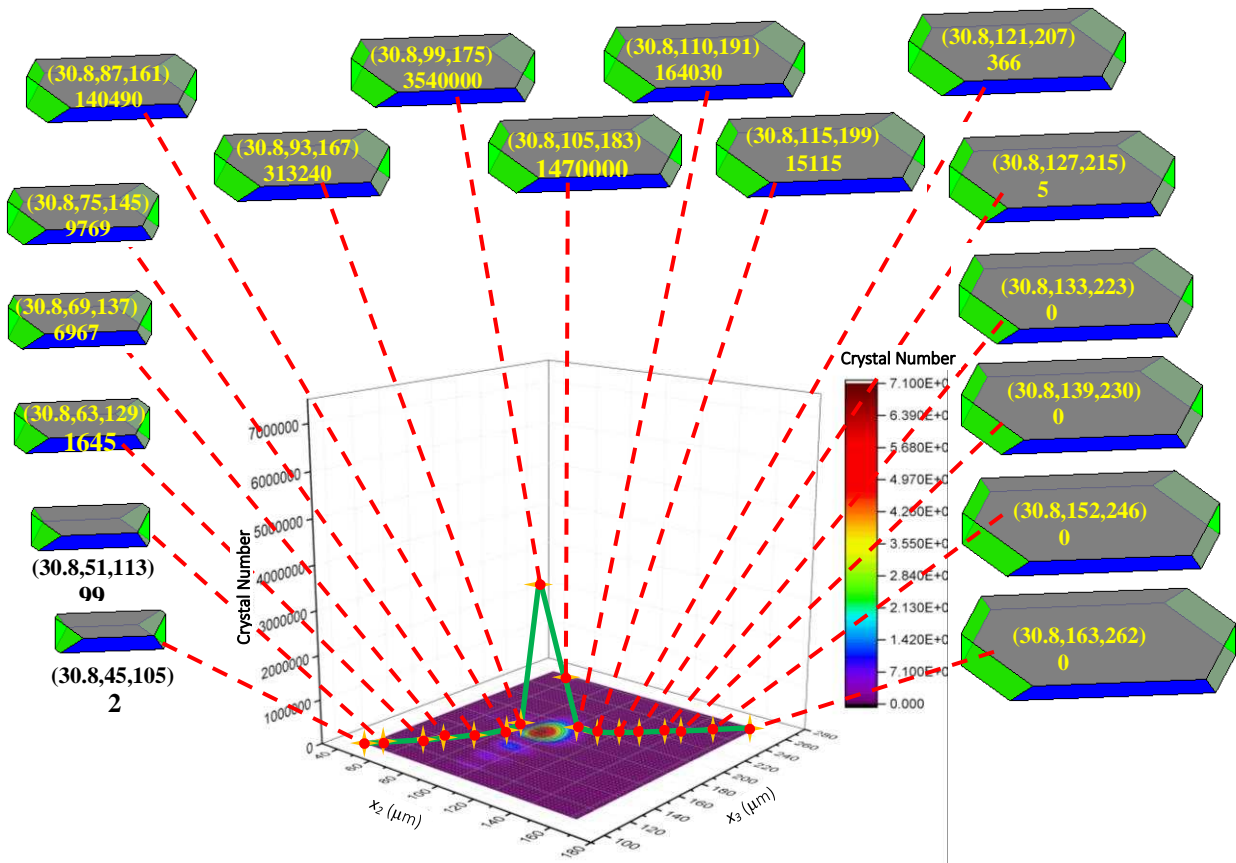


364

365 **Figure 4.** Typical MPB predicted results with CR = 0.5°C/min: (a) solution temperature (T),
366 supersaturation (S), crystal concentration (Cs), (b) evolution of mean normal distances (x_1 , x_2 , x_3), and
367 (c) facet growth rates (G_1 , G_2 , G_3) in (x_1 , x_2 , x_3) face directions.

368

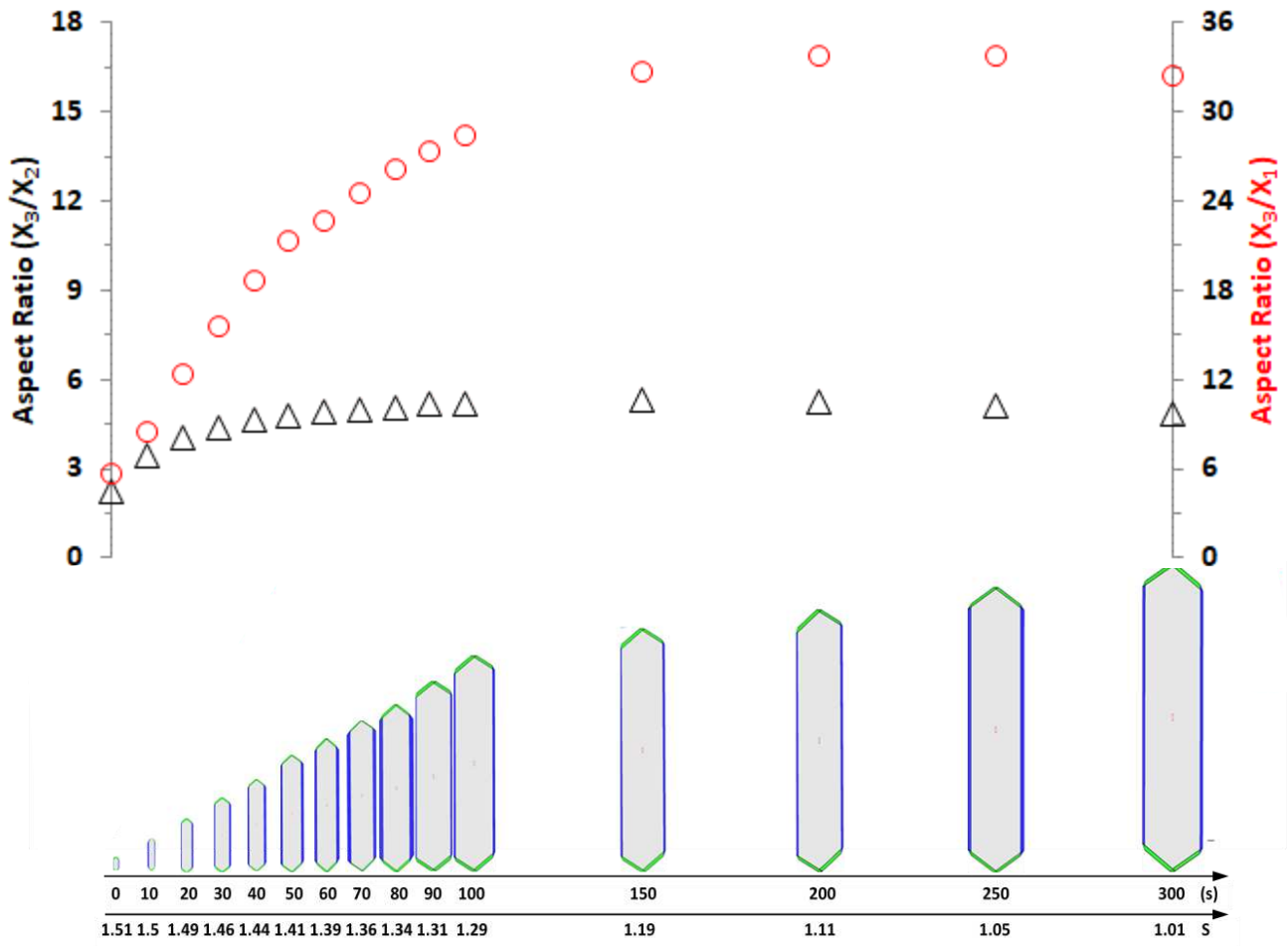
369 Figure 5 presents the typical shape distribution of α -pABA crystals in the final product with a fixed
370 normal distance, x_1 , of 30.8 μm , and other two normal distances (x_2 , x_3) varying from (45 μm , 105
371 μm) to (163 μm , 262 μm). For each normal distances of (30.8, x_2 , x_3), the corresponding crystals
372 shape can be generated based on the definition in Figure 2(b). Therefore, the crystal shape and the
373 number of crystals having this shape were plotted in Figure 5. It demonstrated that the simulated
374 results can provide the accurate and full shape information of the whole population of the crystals.
375 Similarly, the full shape information can be obtained from the simulation results at any individual
376 crystallisation time. Therefore, the evolution map of crystal shape over the whole crystallisation
377 process can be established. Some crystal mean shapes at different processing times are plotted in
378 Figure 6. Due to the fast growth of face {011}, the α -pABA crystals became increasingly needle-like
379 with time. The aspect ratio, X_3/X_2 (where X_2 and X_3 are the mean values of x_2 , x_3 at a crystallisation
380 time), increased from 2.2 (seeds) to 5.3, then reduced slightly to 4.8 (final products). This is due to
381 that the faceted growth rates of face {011}, G_3 , and face {10-1}, G_2 , have a cross-over at the
382 supersaturation of 1.18, i.e. with the further decrease of supersaturation from 1.18, G_3 became smaller
383 than G_2 . Similar trend was found for the aspect ratio, X_3/X_1 (where X_1 is the mean value of x_1), with a
384 much faster increase against time due to that the x_1 grew very slow. Therefore the aspect ratio (X_3/X_1)
385 increases from 6 to over 30.



386

387 **Figure 5.** Typical shape distribution of α -pABA crystals with a fixed normal distance, x_1 , of 30.8
 388 μm , and other two normal distances (x_2 , x_3) varying from (45 μm , 105 μm) to (163 μm , 262 μm).
 389 Note that the values in the brackets are the three normal distances for the individual crystal habit faces
 390 (x_1 , x_2 , x_3) in micrometres together with the number under the brackets which gives the number of
 391 crystals having this specified shape as defined by the normal distances.

392



393

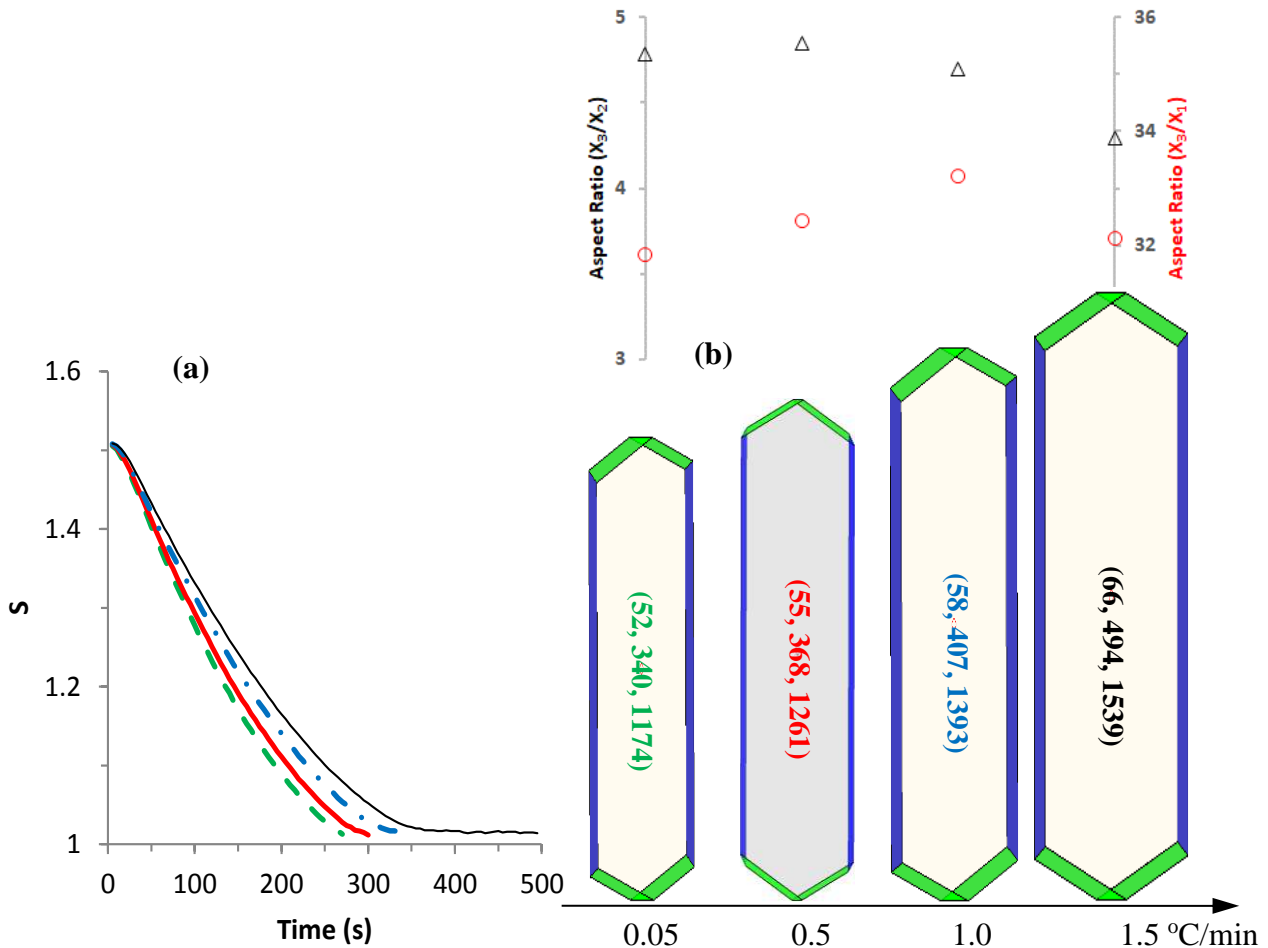
394 **Figure 6.** MPB predicted mean shape evolution of α -pABA crystals crystallised from ethanol with
 395 CR = 0.5°C/min (Aspect ratios: Δ - X_3/X_2 ; \circ - X_3/X_1).

396

397 4.3 Effect of Cooling Rate

398 Figure 7 shows the evolution of supersaturation during crystallisation processes (Figure 7a), and the
 399 final shape/size and their corresponding aspect ratios under four cooling rates (Figure 7b). It can be
 400 seen that the supersaturation decrease with processing time is slower with higher cooling rate (Figure
 401 7a). As the supersaturation is defined as the ratio between solute concentration in the crystalliser at a
 402 given time (temperature) and the solubility of the solute-solvent system at the same given time
 403 (temperature), the evolution of supersaturation during a crystallisation process can be fast or slow
 404 depending on the balance of the solute concentration and solubility. In this study, the higher cooling
 405 rate led to faster decrease of solubility (due to the faster decrease of temperature) than the lower
 406 cooling rate. However, the decrease of solute concentration (due to crystal growth, hence consuming
 407 solute in the solution) does not necessarily follow the same decrease speed. Therefore, if the decrease
 408 of solute concentration is slower than the solubility, the combining effects could result in the slower

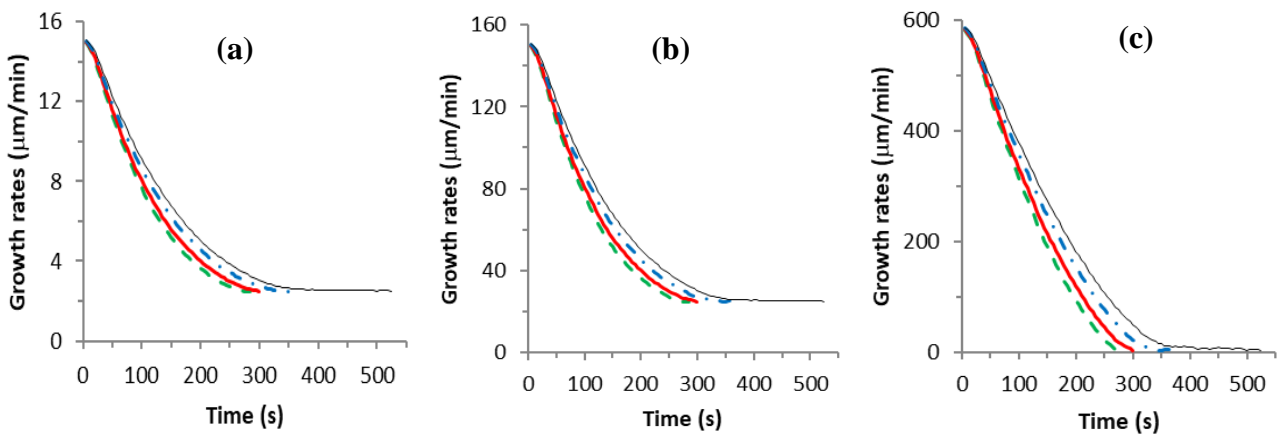
409 reduction of supersaturation with higher cooling rate. The final shape/size under various cooling rates
 410 was found to be similar and the corresponding aspect ratio (X_3/X_2) varied between 4.8 and 4.3 (Figure
 411 7b), which indicates that the variation of cooling rate may not be an effective tool to manipulate
 412 crystal size/shape of final products under the current operating conditions.



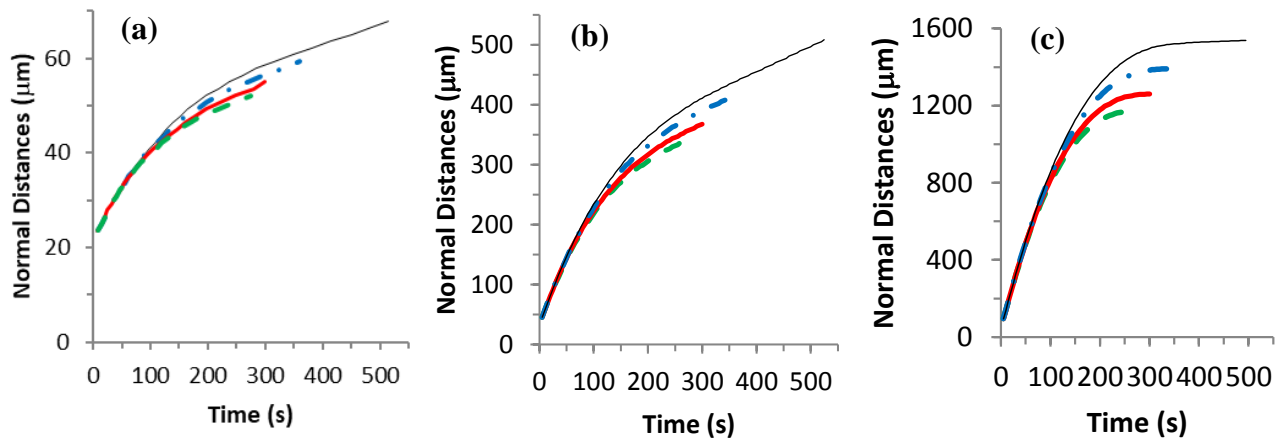
413
 414 **Figure 7.** (a) Supersaturation evolution during crystallisation processes and (b) final mean shape/size
 415 under different cooling rate (CR = 0.05°C/min – dash green line; CR = 0.5°C/min – red line; CR =
 416 1.0°C/min – dash and dot blue line; CR = 1.5°C/min – black line).

417
 418 Figures 8 and 9 illustrate the evolution of faceted growth rates and normal distances, respectively,
 419 during crystallisation processes in face direction of {101}, {10-1} and {011} under different cooling
 420 rates. The face-specific growth rates of the three faces decreased during the process with the speed of
 421 decrease being slower at higher cooling rate. The corresponding normal distances for all three faces
 422 increased faster with the higher cooling rate. By examining the final size/shape of α -pABA crystals
 423 with various cooling rates when supersaturation researched a value of 1.01 (hence no further
 424 crystallisation), the total crystallisation time, final temperature, total crystal mass (yield) and the fine

425 mean size/shape were obtained as shown in Table 2. The total crystal mass in Table 2 was obtained
 426 from $\rho_s \sum_{i=1}^{N_1} \sum_{j=1}^{N_2} \sum_{k=1}^{N_3} [V(x_{1,i}, x_{2,j}, x_{3,k}) \Phi(x_{1,i}, x_{2,j}, x_{3,k})]$, where ρ_s is the density of the crystal,
 427 $V(x_{1,i}, x_{2,j}, x_{3,k})$ is the volume of a crystal with normal distances of $(x_{1,i}, x_{2,j}, x_{3,k})$ calculated based
 428 on the crystals shape shown in Figure 2(b) and $(x_{1,i}, x_{2,j}, x_{3,k})$, and the definitions of other variables
 429 can be found in the Supplementary materials (S3). With the increase of cooling rate from 0.05 to
 430 1.5°C/min in this study, the total process time is almost doubled with the corresponding final
 431 temperature being lowered from about 20°C to 8°C and the yield of α -pABA crystals being increased
 432 about 50%. Furthermore the final crystal size is about 40% larger with CR = 1.5°C/min than
 433 0.05°C/min though the variation of final crystal mean shape (aspect ratio) is not significant.



434
 435 **Figure 8.** Evolution of faceted growth rates during crystallisation processes in face direction of (a)
 436 face {101}, (b) face {10-1} and (c) face {011} under different cooling rate (CR = 0.05°C/min – dash
 437 green line; CR = 0.5°C/min – red line; CR = 1.0°C/min – dash and dot blue line; CR = 1.5°C/min –
 438 black line).



439
 440 **Figure 9.** Evolution of normal distances during crystallisation processes in face direction of (a) face
 441 {101}, (b) face {10-1} and (c) face {011} under different cooling rate (CR = 0.05°C/min – dash green

442 line; CR = 0.5°C/min – red line; CR = 1.0°C/min – dash and dot blue line; CR = 1.5°C/min – black
443 line).

444

445 **Table 2.** MPB modelling results of α -pABA crystallised from ethanol under different CR

CR (°C/min)	Process Time (s)	Final S (-)	Final T (°C)	Final mean (x_1 , x_2 , x_3) (μm)	Total crystal – mass (g)
0.05	270	1.01	20.3	52, 340, 1174	50.7
0.5	300	1.01	18.0	55, 368, 1261	55.0
1.0	340	1.01	14.8	58, 409, 1393	60.5
1.5	495	1.01	8.2	66, 495, 1539	73.1

446

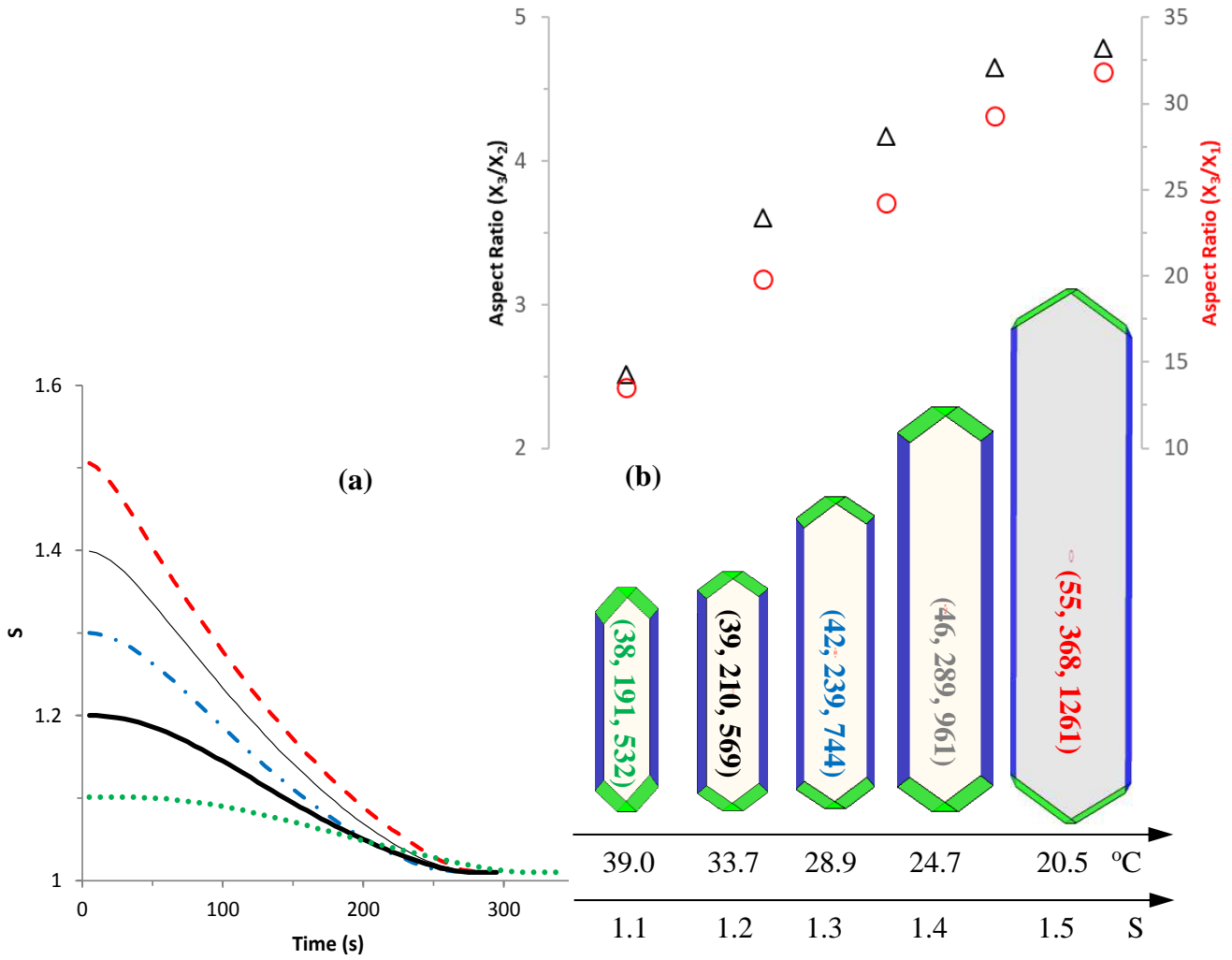
447

448 4.4 Effect of Seeding Temperature

449 In order to investigate the effect of seeding temperature on seeded cooling crystallisation of α -pABA
450 in a batch crystalliser, the seeding temperature (T_{seeds}) was varied from 20.5°C to 39.0°C, which
451 corresponds to seeding supersaturation (S_{seeds}) decreasing from 1.5 to 1.1. The supersaturation
452 evolution during crystallisation processes and the final mean shape/size under different seeding
453 temperature (or seeding supersaturation) are plotted in Figure 10. With a fixed cooling rate of
454 0.5°C/min, as shown in Figure 10a, the supersaturation decreased much faster with lower T_{seeds} (or
455 higher S_{seeds}) than higher T_{seeds} (or lower S_{seeds}). The total process time for various T_{seeds} (or S_{seeds}) did
456 not show significant variation (Table 3). From Figure 10b, it is clear that final mean crystal size with
457 higher T_{seeds} (or lower S_{seeds}) is smaller in size and less needle-like in shape (or lower aspect ratio)
458 (Table 3). When varying of S_{seeds} from 1.1 to 1.5, the aspect ratio (X_3/X_2) was increased from 2.5 to
459 4.8 (Figure 10b).

460 For the evolution of face-specific growth rates and normal distances (x_1 , x_2 , x_3), respectively, during
461 crystallisation processes in face direction of {101}, {10-1} and {011} under different T_{seeds} (or S_{seeds}),
462 the supersaturation decreased slower with higher T_{seeds} (or lower S_{seeds}), hence the facet growth rates
463 for the three individual faces followed the same trend (Figure S.1 in Supplementary materials (S4)).
464 Correspondingly, the normal distances (x_1 , x_2 , x_3) increased against crystallisation time much faster
465 with lower T_{seeds} (or higher S_{seeds}) and also larger actual normal distances (Figure S.2 in
466 Supplementary materials (S4)). Furthermore, this is more significant for the evolution of normal
467 distance of face {011}, i.e. x_3 . As a result, the higher growth rates and bigger actual normal distances
468 with lower T_{seeds} (or higher S_{seeds}) produced much higher yield as shown in Table 3. Therefore, it is
469 not optimal to select an experiment with higher T_{seeds} (or lower S_{seeds}) as the resultant yield would be

470 unacceptably low albeit from these conditions the final crystal shape would be expected to be less
 471 needle-like (smaller aspect ratio).



472
 473 **Figure 10.** (a) Supersaturation evolution during crystallisation processes and (b) final mean
 474 shape/size under different seeding temperature (T_{seeds}) (or supersaturations (S_{seeds})) ($T_{seeds} = 20.5^\circ\text{C}$
 475 (or $S_{seeds} = 1.5$) – dash red line; $T_{seeds} = 24.7^\circ\text{C}$ (or $S_{seeds} = 1.4$) – thin black line; $T_{seeds} = 28.9^\circ\text{C}$ (or
 476 $S_{seeds} = 1.3$) – dash and dot blue line; $T_{seeds} = 33.7^\circ\text{C}$ (or $S_{seeds} = 1.2$) – black line; $T_{seeds} = 39.0^\circ\text{C}$ (or
 477 $S_{seeds} = 1.1$) – dot green line).

478
 479
 480
 481
 482

483 **Table 3.** MPB modelling results of α -pABA crystallised from ethanol under different seeding
 484 temperature (T_{seeds}) (or seeding supersaturation (S_{seeds}))

Seeding point – T_{seeds} ($^{\circ}\text{C}$)	S_{seeds} (-)	Time (s)	Final S (-)	Final T ($^{\circ}\text{C}$)	Final means (x_1, x_2, x_3) (μm)	Total crystal – mass (g)
39.0	1.1	290	1.01	36.55	37.9, 191, 376	17.5
33.7	1.2	260	1.01	31.5	39.3, 210, 568	28.5
28.9	1.3	250	1.01	26.85	42.1, 239, 744	38.0
24.7	1.4	265	1.01	22.47	46.4, 289, 961	46.5
20.5	1.5	300	1.01	18.0	55, 368, 1261	55.0

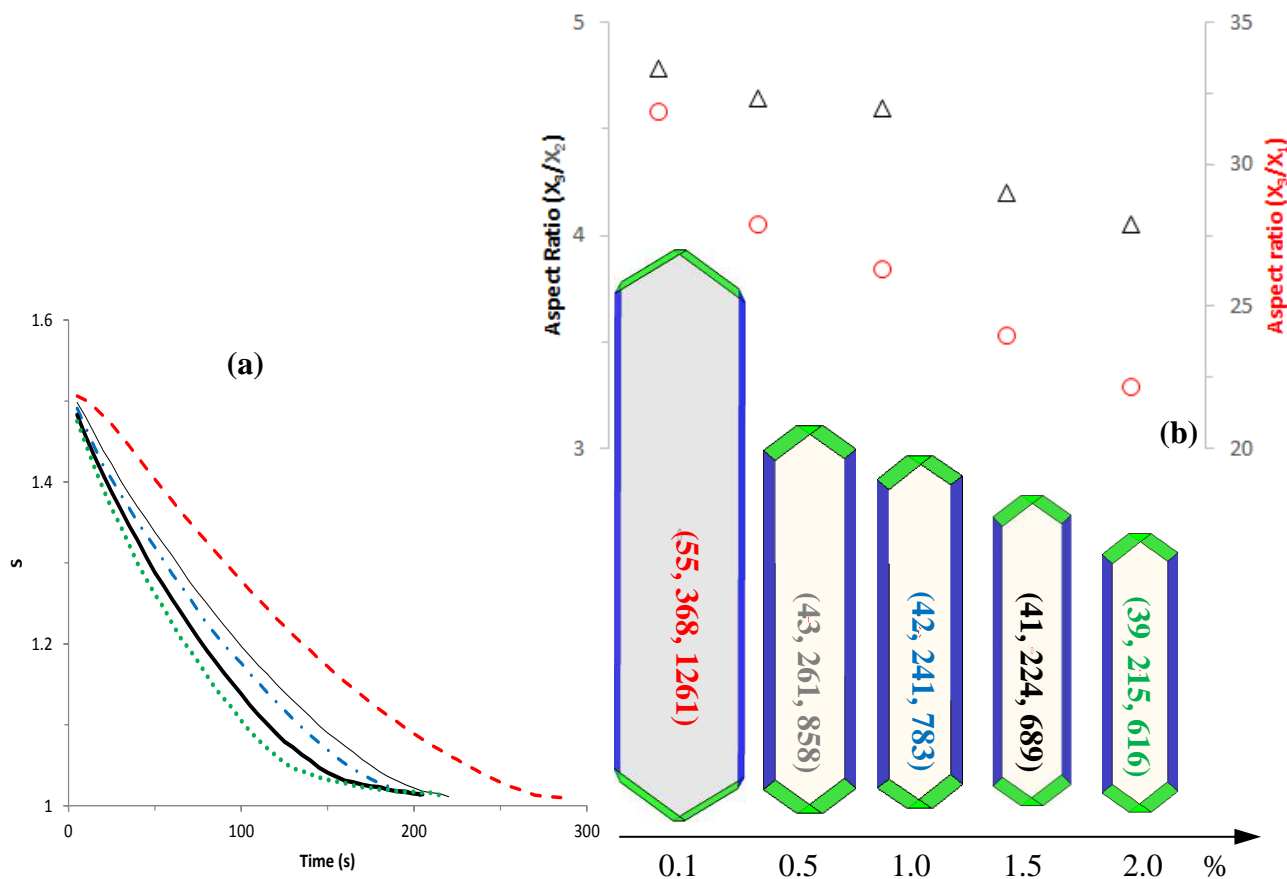
485

486

487 **4.5 Effect of Seed Loading**

488 Figure 11 shows the evolution of supersaturation during crystallisation processes (Figure 11a), and
 489 the final mean shape/size and their corresponding aspect ratios (Figure 11b) under five different seed
 490 loadings. With higher seed loading under the same Gaussian-like size/shape distribution (same mean
 491 values and same standard deviations), the total number of crystals becomes proportionally larger.
 492 Therefore, the total crystal surface area for crystal growth is predicted to increase with the increase
 493 of seed loading, hence solute concentration reduces faster, leading to faster supersaturation decrease
 494 (Figure 11a). As the total number of seeds is higher with higher seed loading, the solute available for
 495 each seed is less accordingly. Therefore, as shown in Figure 11b, the final mean crystal is smaller in
 496 size and also less needle-like in shape (or aspect ratio). When seed loading increases from 0.1% to
 497 2.0% (by mass), the MPB simulation results show that the aspect ratio (X_3/X_2) decreases almost
 498 linearly with a slope of -0.4 and intercept of 4.8 (Figure 11b).

499 The evolution of faceted growth rates (Figure S.3 in Supplementary materials (S5)) and face normal
 500 distances (Figure S.4 in Supplementary materials (S5)) during crystallisation processes on the {101},
 501 {10-1} and {011} faces under different seed loadings demonstrated that as the increase of seed
 502 loading resulted in the faster decrease of supersaturation (Figure 11a), the faceted growth rates (G_1 ,
 503 G_2 , G_3) also decrease faster (Figure S.3) with the corresponding normal distances being in slower
 504 increase (Figure A.4). The final temperature and yield did not have significant variation for the
 505 simulated range of seed loadings (Table 4). However, the crystal size of final product is predicted to
 506 be smaller with less needle-like in shape when seed loading is increased. Therefore, seed loading can
 507 be an effective tool for optimising and controlling crystal size/shape distribution using MPB
 508 approach.



509

510 **Figure 11.** (a) Supersaturation evolution during crystallisation processes and (b) final mean
 511 shape/size under different seed loading (X_{seeds}) ($X_{seeds} = 0.1\%$ – dash red line; $X_{seeds} = 0.5\%$ – thin
 512 black line; $X_{seeds} = 1.0\%$ – dash and dot blue line; $X_{seeds} = 2.0\%$ – black line; $X_{seeds} = 5.0\%$ – dot green
 513 line).

514

515 **Table 4.** MPB modelling results of α -pABA crystallised from ethanol under different seed loading
 516 (X_{seeds})

X_{seeds} (% mass)	Time (s)	Final S (-)	Final T ($^{\circ}$ C)	Final means (x_1, x_2, x_3) (μ m)	Total crystal – mass (g)
0.1	270	1.01	18.0	55, 368, 1261	55.0
0.5	220	1.01	18.7	43.6, 261, 858	54.5
1.0	205	1.01	18.8	42.1, 241, 783	55.0
2.0	205	1.01	18.8	40.7, 224, 689	56.3
5.0	215	1.01	18.7	39.3, 215, 616	57.4

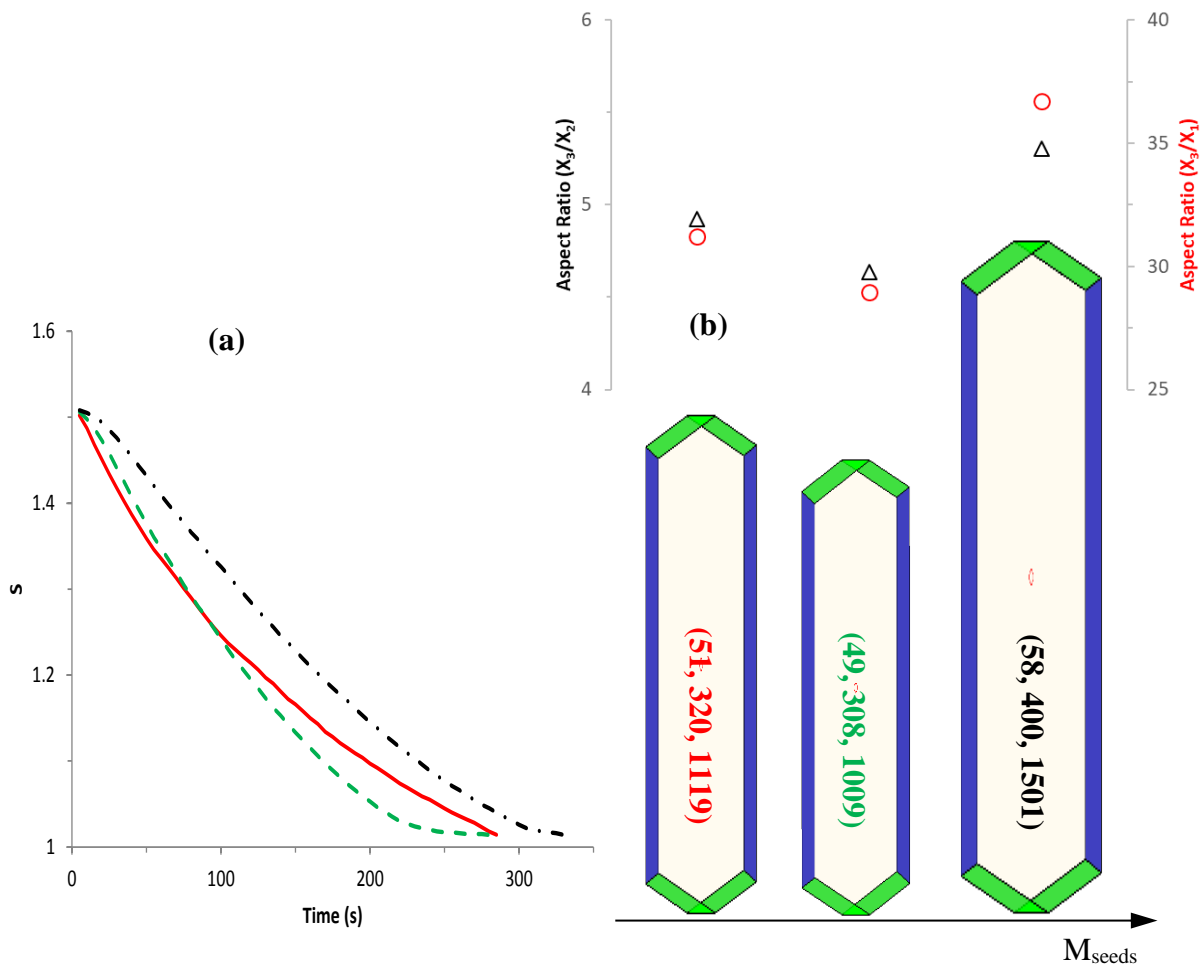
517

518

519

520 **4.6 Effect of Seed Mean Shape**

521 To investigate the effect of seed mean shape on crystal size/shape distribution during α -pABA
 522 crystallisation process, three different mean shape were used for establishing seeds size/shape
 523 distribution (e.g. Figure 3a): mean normal distances (x_1, x_2, x_3) of (22, 27, 6 μm), (22, 27, 40 μm) and
 524 (22, 27, 131 μm) with fixed standard deviations of $(\sigma_{x_1}, \sigma_{x_2}, \sigma_{x_3}) = 8 \mu\text{m}$. Figure 12 shows the
 525 supersaturation evolution during crystallisation processes and the final mean shape/size under
 526 different seed mean shape. With more needle-like seeds, the total number of seeds (under the same
 527 seed loading) was found to be slightly smaller, hence leading to slower decrease of supersaturation
 528 (Figure 12a). However, the simulated final crystal size is found to be bigger with slightly higher
 529 aspect ratio (Figure 12b). Similarly, the faceted growth rates follow the same trend of decrease (Figure
 530 S.5 in Supplementary materials (S6)) and the normal distances (x_1, x_2, x_3) have the similar trend of
 531 increase with crystallisation time (Figure S.6 in Supplementary materials (S6)). The final temperature
 532 and yield do not present significant variation for the three seed mean shape (Table 5).



533 **Figure 12.** (a) supersaturation evolution during crystallisation processes and (b) final mean shape/size
 534 under different seed mean shape (M_{seeds}) with standard deviations of $(\sigma_{x_1}, \sigma_{x_2}, \sigma_{x_3}) = 8 \mu\text{m}$ ($M_{\text{seeds}} =$

535 (22, 27, 6 μm) – red line; $M_{\text{seeds}} = (22, 27, 40 \mu\text{m})$ – dash green line; $M_{\text{seeds}} = (22, 27, 131 \mu\text{m})$ – dash
 536 and dot black line).

537

538 **Table 5.** MPB modelling results of α -pABA crystallised from ethanol under different seed mean
 539 shape (M_{seeds})

$M_{\text{seeds}} (x_1, x_2, x_3) (\mu\text{m})$	Seeds standard deviations $(\sigma_{x_1}, \sigma_{x_2}, \sigma_{x_3}) (\mu\text{m})$	Time (s)	Final S (-)	Final T ($^{\circ}\text{C}$)	Final means $(x_1, x_2, x_3) (\mu\text{m})$	Total crystal – mass (g)
22, 27, 6	8, 8, 8	285	1.01	18.1	50.7, 320, 1119	54.6
22, 27, 40	8, 8, 8	280	1.01	18.18	49.3, 308, 1009	54.4
22, 27, 131	8, 8, 8	330	1.01	17.76	57.9, 400, 1501	55.2

540

541

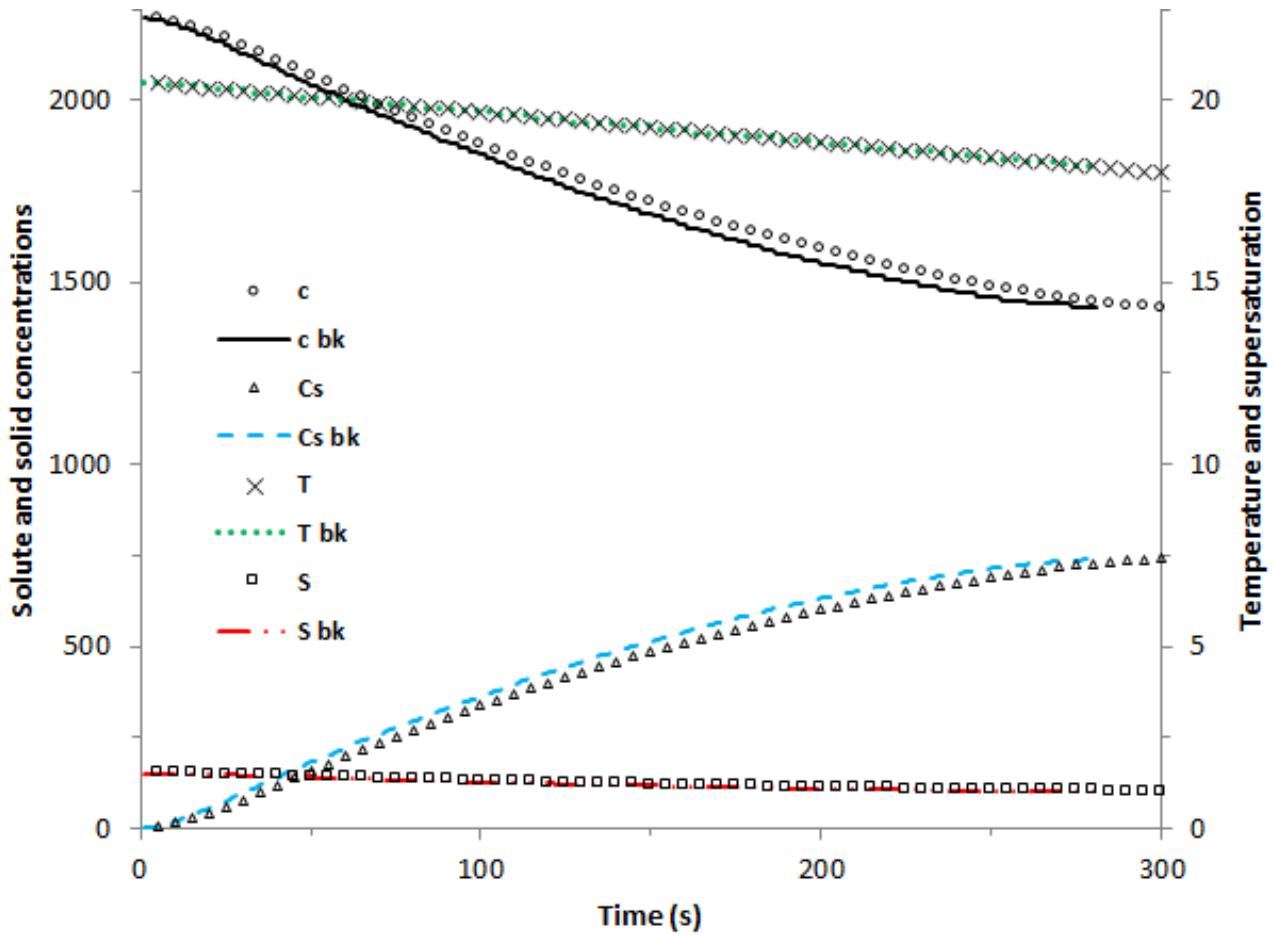
542 4.7 Effect of Broken Seeds

543 Theoretically seeds may be treated as perfect crystals with the required size/shape distribution.
 544 However, in practice, seeds are usually collected from small scale and well-controlled crystallisation
 545 processes, then followed by the necessary washing, filtration and drying, all processes which might
 546 expect to provide some extent of breakage/damage to the obtained seeds. In order to obtain seeds with
 547 the required size, milling/sieving processes may be used, which understandably will generate broken
 548 seeds at very high extent. In this section, the MPB model was used to simulate the behaviour of the
 549 broken seeds during crystallisation processes. All operating conditions are as the same as those from
 550 the base case (section 4.2) with the size/shape distribution of broken seeds as shown in Figure 3b.
 551 The broken face (010) should be rough with most possibly an RIG growth mechanism. In this study,
 552 the facet growth rate of face (010) was estimated to be two times of that for face {011}, G_3 . It should
 553 be noted that the more accurate growth rate and growth mechanism for the broken face (010) are
 554 needed through the use of molecular modelling and/or experimental measurements.

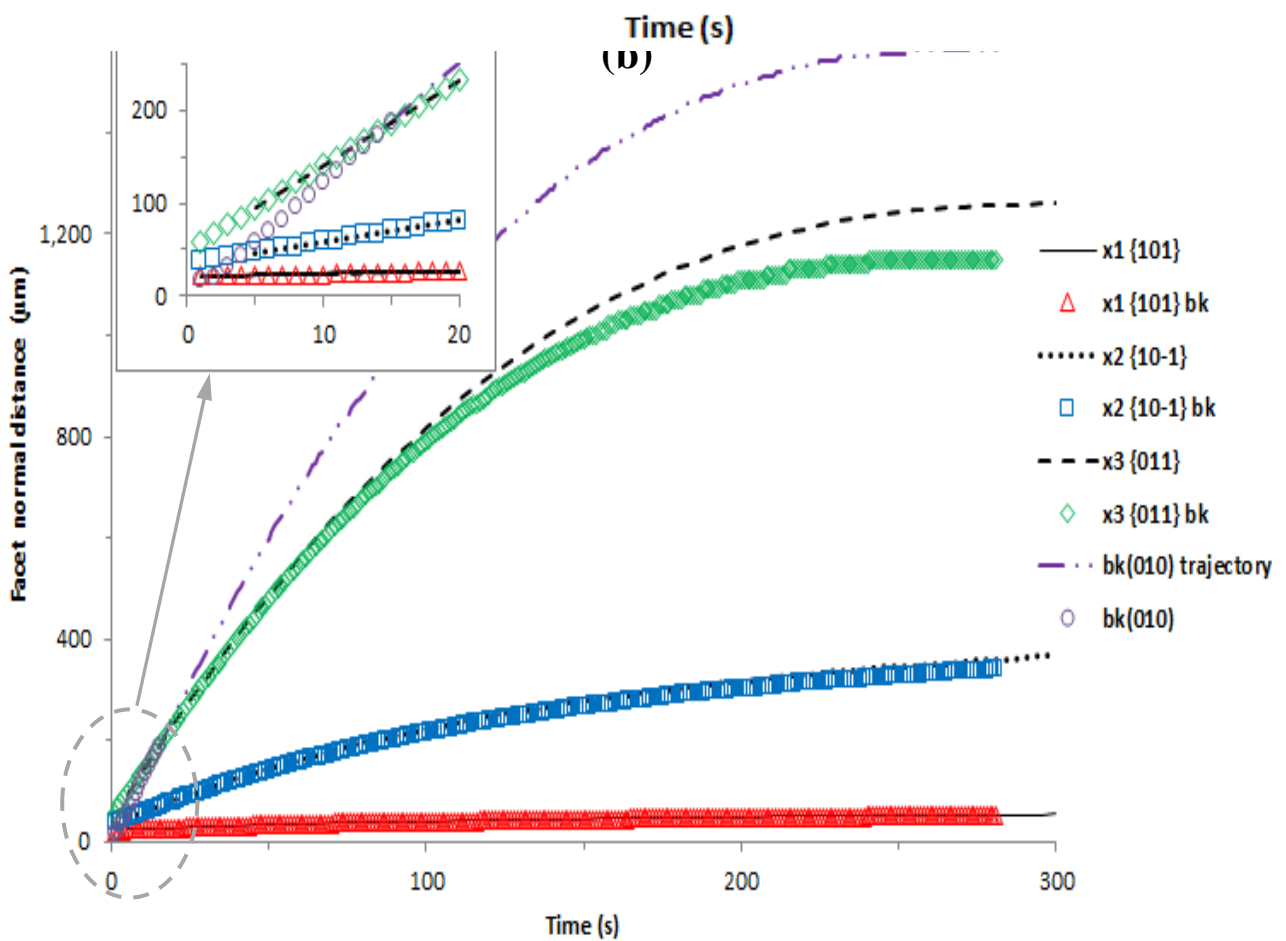
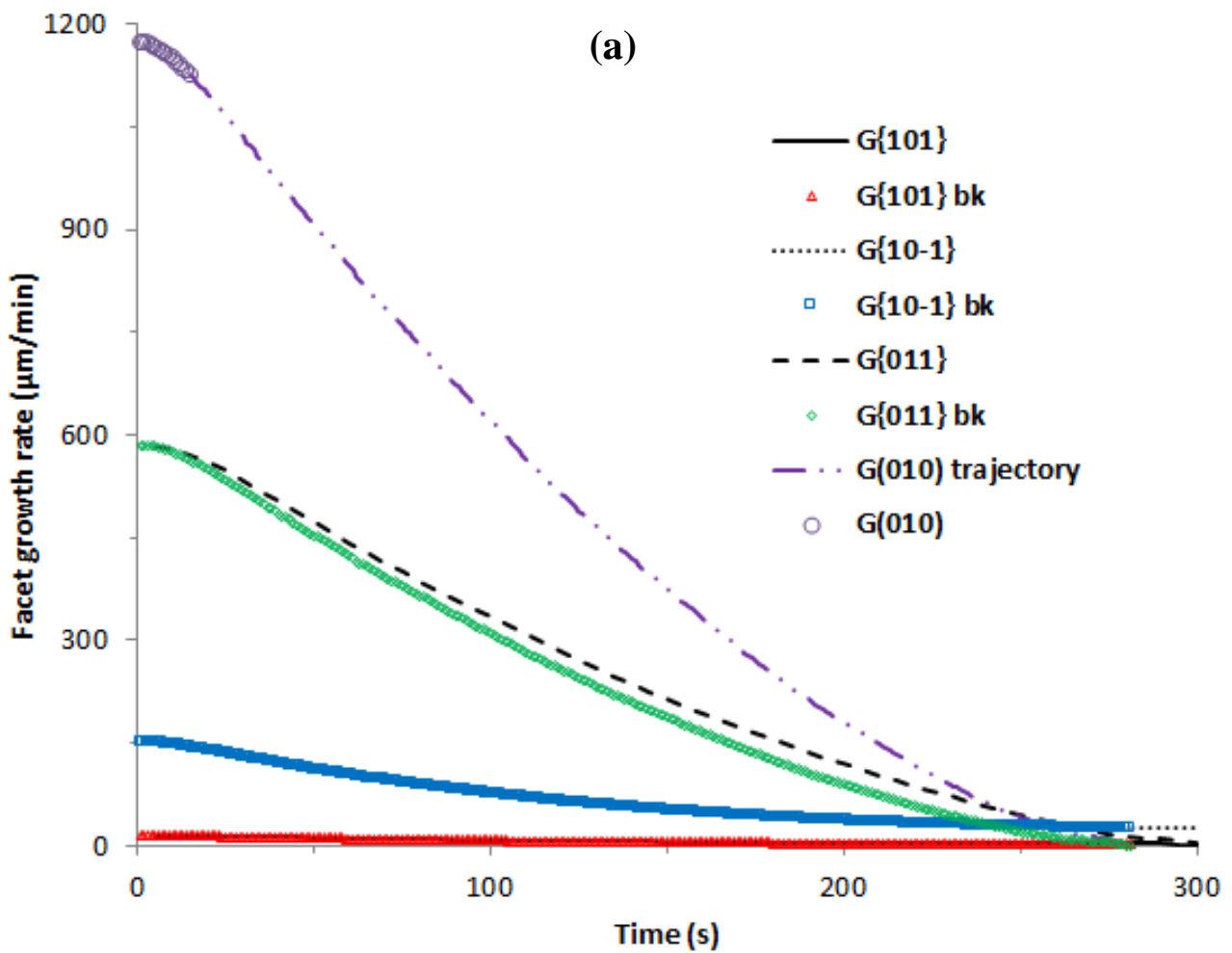
555 Figure 13 shows the solution temperature, supersaturation, solute concentration and solid
 556 concentration during crystallisation processes with perfect seeds or broken seeds. With the same
 557 cooling rate ($0.5^{\circ}\text{C}/\text{min}$), supersaturation with broken seeds decreased slightly faster, hence reaching
 558 the supersaturation value of 1.01 earlier ($\sim 28\text{s}$). Correspondingly, solute concentration dropped at a
 559 higher speed and solid concentration increased faster.

560 Figures 14 presents the faceted growth rates in the directions of faces {101}, {10-1} and {011}, and
 561 also broken face (010) with its trajectory, and the corresponding evolution of normal distances for the
 562 mentioned four faces. MPB simulations revealed that the broken face (010) grew very fast, then

563 disappeared after about 15 s (Figure 14b). The facet normal distances, in particular x_3 for face {011},
 564 increased slower at the late stage of the crystallisation process with broken seeds. The main
 565 contributors are both broken seeds (shorter in size and higher number of seeds) and the faster decrease
 566 of supersaturation (also faster decrease of growth rate of face {011}) (Figure 14a)).



567
 568 **Figure 13.** Solution temperature (T and T_{bk}), supersaturation (S and S_{bk}), solute concentration (c and
 569 c_{bk}) and solid concentration (C_s and $C_{s,bk}$) during crystallisation processes with the operating
 570 conditions of the base case and broken seeds (Symbols – perfect seed crystals; Lines – broken seed
 571 crystals; bk – broken seeds).

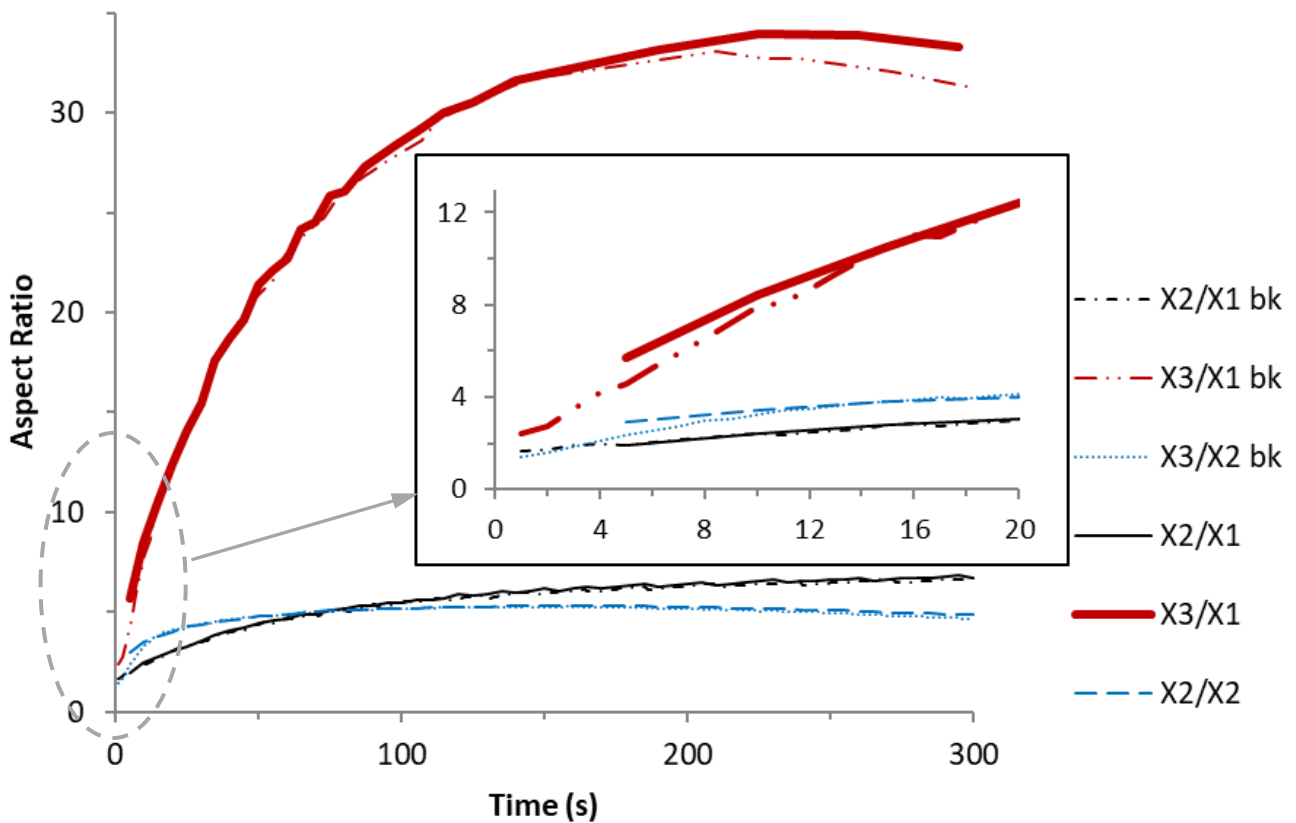


573 **Figure 14.** Faceted growth rates (a) and Normal distances (b) in the face directions of face {101}
 574 (solid line – perfect seed crystals; \triangle – broken seed crystals), face {10-1} (dot line – perfect seed
 575 crystals; \square – broken seed crystals) and face {011} (Dash line – perfect seed crystals; \diamond – broken
 576 seed crystals), and also broken face (010) (dash and dots line) with its trajectory (\circ) during
 577 crystallisation processes with the operating conditions of the base case.

578

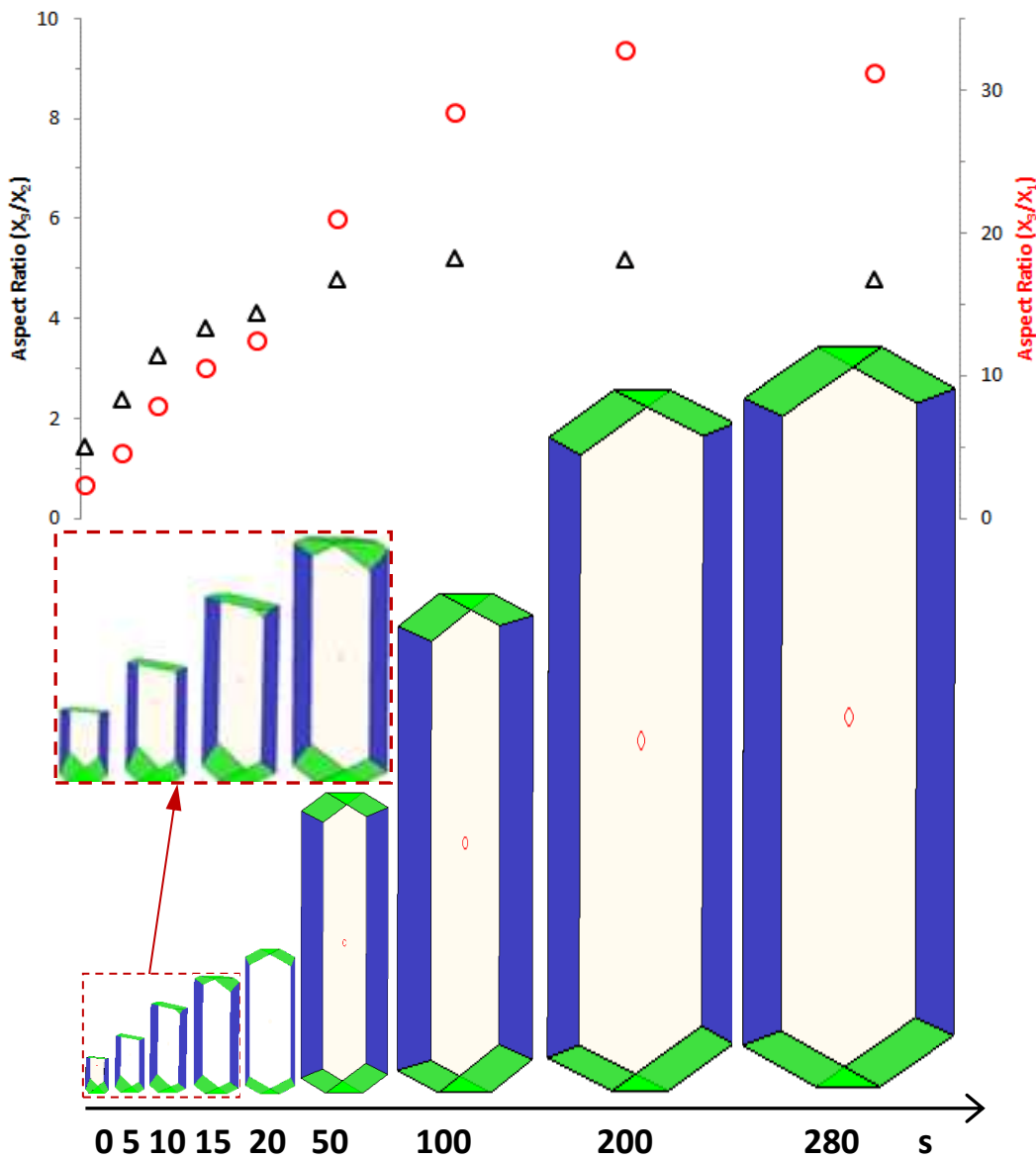
579 Figures 15 and 16 present the evolution of aspect ratios (X_3/X_2 , X_3/X_1 , X_2/X_1) during crystallisation
 580 process for both perfect seeds and broken seeds, and crystal mean shape evolution and aspect ratios
 581 at several typical time points for broken seeds, respectively. Note that X_1 , X_2 and X_3 are the mean
 582 values of x_1 , x_2 , x_3 at a crystallisation time. The aspect ratios (X_3/X_2 and X_3/X_1) increased fast to the
 583 values for perfect seeds after about 15 s (Figure 15) with the broken face (010) being disappearance
 584 (Figure 16).

585



586 **Figure 15.** Evolution of aspect ratios during crystallisation process with perfect and broken seeds.

587



588

589 **Figure 16.** Crystal mean shape evolution and aspect ratios at some typical time instances (0, 5, 10,
 590 15, 20, 50, 100, 200, 300 s). Note that the broken face (010) grew fast and disappeared in about 15 s.

591

592 **5. Conclusions**

593 In this study, the MPB models were applied for simulating pharmaceutical crystallisation processes
 594 as illustrated through a case study of α -pABA crystals crystallised from ethanolic solution under a
 595 wide-range of operating conditions notably cooling rate, seeding temperature (seeding
 596 supersaturation), seed loading, seeds shape/size (including broken seeds). The MPB simulations
 597 captured the shape-dependent behaviour of the crystallisation processes under these operating
 598 conditions with the effect of defining the impact of these processing variables on the crystal size/shape
 599 distribution and their evolution.

600 Within the operating conditions used for MPB simulations, faster cooling was shown to increase the
601 crystallisation time to reach solution equilibrium conditions, i.e. $S = 1$, with the corresponding
602 finishing solution temperature being much lower, hence leading to higher yield and larger final crystal
603 size. Although higher seeding temperatures (hence lower seeding supersaturations) was found to
604 produce less needle-like α -pABA crystals, the yield was much lower than that at lower seeding
605 temperatures. On the other hand, higher seed loading was found to generate smaller sized crystals
606 which were less needle-like in shape while having very similar yields. This indicated that seed loading
607 could be a useful control variable for using MPB to obtain the pre-desired crystal size/shape
608 distribution. For the case with broken seeds, the fractured seed surfaces were found to grow fast and
609 hence disappear from the external morphology during the crystallisation process. Such simulations
610 could have wide applications in pharmaceutical industry mindful that seeds used often exhibit some
611 kind of breakage and/or damage during seed preparation processes, e.g. through milling.

612 Further research should include the consideration of the effect of primary nucleation (i.e., without
613 seeds) and together with that of secondary nucleation through surface breeding from seeds, face-
614 specific crystal agglomeration and breakage into the MPB model. This will involve first-principle
615 based research on crystal morphology and surface chemistry, solid/solution interface (including the
616 interactions of crystal-crystal, crystal-solute and crystal-solvent), solution chemistry, etc. Through
617 these, combining the MPB model with computational fluid dynamics for crystalliser hydrodynamics
618 and multi-zonal modelling will form a powerful digital design framework for pharmaceutical
619 crystallisation to manufacture crystals with pre-desired properties, hence delivering targeted
620 medicines.

621

622 **Acknowledgments**

623 The authors gratefully acknowledge the financial support by the UK's Advanced Manufacturing
624 Supply Chain Initiative 'Advanced Digital Design of Pharmaceutical Therapeutics' (ADDoPT)
625 project (Grant No. 14060). This work also builds upon research on morphological modelling
626 supported by EPSRC grant 'HABIT – Crystal morphology from crystallographic and growth
627 environment factors' through EPSRC grant EP/I028293/1 and the Synthonic Engineering programme
628 supported by Pfizer, Boeringer-Ingellheim, Novartis and Syngenta. We also gratefully acknowledge
629 EPSRC for the support of crystallization research at Leeds and Manchester through the Critical Mass
630 grant 'Molecules, Clusters and Crystals' (Grant references EP/IO14446/1 and EP/IO13563/1).

631

632 Declarations of interest: none

634 **References**

- 635 BELL, J. 2017. Life Sciences Industrial Strategy - A report to the Government from the life sciences
636 sector (<https://www.gov.uk/government/publications/life-sciences-industrial-strategy>).
- 637 CAMACHO, D. M., ROBERTS, K. J., MULLER, F., THOMAS, D., MORE, I. & LEWTAS, K.
638 2016. Morphology and Growth of Methyl Stearate as a Function of Crystallization
639 Environment. *Crystal Growth & Design*, 17, 2088-2095.
- 640 CLYDESDALE, G., DOCHERTY, R. & ROBERTS, K. J. 1991. Habit - a program for predicting the
641 morphology of molecular-crystals. *Computer Physics Communications*, 64, 311-328.
- 642 CLYDESDALE, G., ROBERTS, K. J. & DOCHERTY, R. 1996. HABIT95, Quantum Chemistry
643 Program Exchange, Program no. 670, Bloomington, IN 47405, USA.
- 644 HULBURT, H. M. & KATZ, S. 1964. Some Problems in Particle Technology - a Statistical
645 Mechanical Formulation. *Chemical Engineering Science*, 19, 555-574.
- 646 KUVADIA, Z. B. & DOHERTY, M. F. 2013. Reformulating Multidimensional Population Balances
647 for Predicting Crystal Size and Shape. *AIChE Journal*, 59, 3468-3474.
- 648 LOVETTE, M. A., BROWNING, A. R., GRIFFIN, D. W., SIZEMORE, J. P., SNYDER, R. C. &
649 DOHERTY, M. F. 2008. Crystal Shape Engineering. *Industrial & Engineering Chemistry
650 Research*, 47, 9812-9833.
- 651 MA, C. Y. & ROBERTS, K. J. 2018. Combining Morphological Population Balances with Face-
652 Specific Growth Kinetics Data to Model and Predict the Crystallization Processes for
653 Ibuprofen. *Ind Chem Eng Res*, 57, 16379-16394.
- 654 MA, C. Y., WANG, X. Z. & ROBERTS, K. J. 2008. Morphological population balance for modelling
655 crystal growth in individual face directions. *AIChE Journal*, 54, 209-222.
- 656 MAIER, J. 2017. Made Smarter Review 2017 ([https://www.gov.uk/government/publications/made-
657 smarter-review](https://www.gov.uk/government/publications/made-smarter-review)).
- 658 MARCHAL, P., DAVID, R., KLEIN, J. P. & VILLERMAUX, J. 1988. Crystallization and
659 precipitation engineering .1. An efficient method for solving population balance in
660 crystallization with agglomeration. *Chemical Engineering Science*, 43, 59-67.
- 661 NGUYEN, T. T. H., HAMMOND, R. B., ROBERTS, K. J., MARZIANO, I. & NICHOLS, G. 2014.
662 Precision measurement of the growth rate and mechanism of ibuprofen {001} and {011} as a
663 function of crystallization environment. *CrystEngComm*, 16, 4568-4586.
- 664 PICKERING, J., HAMMOND, R. B., RAMACHANDRAN, V., SOUFIAN, M. & ROBERTS, K. J.
665 2017. Synthonic Engineering Modelling Tools for Product and Process Design. In:
666 ROBERTS, K. J., DOCHERTY, R., TAMURA, R. (ed.) *Engineering Crystallography: From
667 Molecule to Crystal to Functional Form*. Dordrecht: Springer.
- 668 PUEL, F., FEVOTTE, G. & KLEIN, J. P. 2003. Simulation and analysis of industrial crystallization
669 processes through multidimensional population balance equations. Part 1: a resolution
670 algorithm based on the method of classes. *Chemical Engineering Science*, 58, 3715-3727.
- 671 RAMKRISHNA, D. & MAHONEY, A. W. 2002. Population balance modeling. Promise for the
672 future. *Chemical Engineering Science*, 57, 595-606.
- 673 RANDOLPH, A. D. & LARSON, M. A. 1988. *Theory of particulate processes: Analysis and
674 techniques of continuous crystallization*, Academic Press, London.
- 675 ROSBOTTOM, I. 2016. The Influence of the Intermolecular Synthons on the Molecular Aggregation,
676 Polymorphism, Crystal Growth and Morphology of p-Aminobenzoic Acid Crystals from
677 Solution. PhD, PhD Thesis, University of Leeds, UK.
- 678 ROSBOTTOM, I., MA, C. Y., TURNER, T. D., O'CONNELL, R. A., LOUGHREY, J., SADIQ, G.,
679 DAVEY, R. J. & ROBERTS, K. J. 2017. Influence of Solvent Composition on the Crystal
680 Morphology and Structure of p-Aminobenzoic Acid Crystallized from Mixed Ethanol and
681 Nitromethane Solutions. *Crystal Growth & Design*, 17, 4151-4161.

682 ROSBOTTOM, I., ROBERTS, K. J. & DOCHERTY, R. 2015. The solid state, surface and
683 morphological properties of p-aminobenzoic acid in terms of the strength and directionality
684 of its intermolecular synthons. *CrystEngComm*, 17, 5768-5788.

685 SHAMPINE, L. F. & WATTS, H. A. Subroutine RKF45. In: G. E. FORSYTHE, M. A. M., C. B.
686 MOLER, ed. *Computer Methods for Mathematical Computations*, 1977 Englewood Cliffs, N.
687 J.: Prentice-Hall, 135-147.

688 SULLIVAN, R. A., DAVEY, R. J., SADIQ, G., DENT, G., BACK, K. R., TER HORST, J. H.,
689 TOROZ, D. & HAMMOND, R. B. 2014. Revealing the Roles of Desolvation and Molecular
690 Self-Assembly in Crystal Nucleation from Solution: Benzoic and p-Aminobenzoic Acids.
691 *Crystal Growth & Design*, 14, 2689-2696.

692 TOROZ, D., ROSBOTTOM, I., TURNER, T. D., CORZO, D. M. C., HAMMOND, R. B., LAI, X.
693 & ROBERTS, K. J. 2015. Towards an understanding of the nucleation of alpha-para amino
694 benzoic acid from ethanolic solutions: a multi-scale approach. *Faraday Discussions*, 179, 79-
695 114.

696 TURNER, T. D., NGUYEN, T. T. H., NICHOLSON, P., BROWN, G., HAMMOND, R. B.,
697 ROBERTS, K. J. & MARZIANO, I. 2019. A temperature-controlled single-crystal growth
698 cell for the in situ measurement and analysis of face specific growth rates. *Journal of Applied*
699 *Crystallography*, 52, 463-467.

700 ZHANG, Y. C. & DOHERTY, M. F. 2004. Simultaneous prediction of crystal shape and size for
701 solution crystallization. *AIChE Journal*, 50, 2101-2112.

702

Supplementary Materials

This supplementary provides the mini-review of population balance (PB) models (S1), face-specific crystal growth kinetics (S2), the solution method of morphological PB (S3) and the additional simulation results of the evolution of face-specific growth rates and normal distances under different seeding temperature (S4), seed loading (S5) and seed mean shape (S6), and the references for supplementary materials (S7).

S1. Mini-review of PB models

For modelling the evolution of a population of crystals during crystallisation processes, one-dimensional (1D) population balance (PB) approach (e.g., (Alvarez and Myerson, 2010, Caillet et al., 2007, Fevotte et al., 2007, Garside, 1985, Gerstlauer et al., 2006, Hounslow et al., 2005, Li et al., 2013, Liu and Li, 2014, Marchal et al., 1988, Menon et al., 2005, Patience et al., 2004, Rawlings et al., 1992, Temmel et al., 2016, Ulbert and Lakatos, 2005, Ward et al., 2006)), using a characteristic size, such as length (e.g., (Vetter et al., 2014, Ward et al., 2011, Zhang and Doherty, 2004)), diameter or radius of a volume equivalent sphere (e.g., (Marchal et al., 1988)) to simplify a faceted crystal, was used and still being used widely. Two-dimensional (2D) PB method was developed to account for needle-/rod-/plate-like crystals (e.g., (Briesen, 2009, Gunawan et al., 2004, Ma et al., 2007, Oullion et al., 2007, Puel et al., 2003a, Puel et al., 2003b, Ramkrishna and Mahoney, 2002, Sato et al., 2008, Shi et al., 2006)), whilst the introducing a volumetric shape factor into the 1D (or 2D) PB is to more accurately represent the crystal volume (Zhang and Doherty, 2004). However, using a 1D PB with the assumptions that all crystal faces have the same surface chemistry, growth mechanism and a constant relative growth rate ratio amongst all faces, the evolution of crystal size and shape could be represented (e.g., Doherty and co-workers (Lovette et al., 2008, Zhang and Doherty, 2004, Kuvadia and Doherty, 2013)). Critically, a 1D PB assumes that the crystal morphology does not change during growth, i.e. that the ratio of the growth rates between the different faces is constant. The aspect was first addressed by Ma et al. (Ma et al., 2008), followed by other researchers (e.g., (Borchert et al., 2009, Borchert and Sundmacher, 2012, Chakraborty et al., 2010, Kwon et al., 2013, Kwon et al., 2014, Liu et al., 2013, Liu et al., 2010b, Liu et al., 2010a, Ma et al., 2016, Ma and Roberts, 2018, Ma and Wang, 2008, Ma and Wang, 2012, Wan et al., 2009, Wang and Ma, 2009, Wang et al., 2008, Majumder and Nagy, 2013, Kuvadia and Doherty, 2013)). A crystal has its face forms identified as $\{hkl\}$. For a cubic crystal, it only has one form but 6 faces. For a potash alum crystal, it has 3 forms but 24 faces. The MPB uses crystal morphology to identify crystal forms with each form being treated as an independent variable (crystal face-to-centre distance) and the total

736 number of forms determines the number of dimensions of the MPB equation. It can be assumed that
 737 the faces of each form have the same surface chemistry, growth mechanism/rate and also other
 738 physical/chemical properties. See more detail in e.g. (Ma et al., 2008). The MPB not only provides a
 739 direct tool for optimisation and control of both final crystal size and shape but enables control of the
 740 particle properties and processing.

741

742 **S2. Face-specific crystal growth kinetics**

743 The kinetics of a defined crystal growth interface as a function of supersaturation can generally be
 744 described by a number of well-known models including power law (Garside, 1985), birth & spread
 745 (B&S) and Burton-Cabrera-Frank (BCF) models (Burton et al., 1951). During crystallisation
 746 processes in a crystal growth cell and other crystallisers, crystal growth rate is very much a two-step
 747 kinetic process encompassing a balance between the incorporation of growth units onto the crystal
 748 surface and the diffusion by mass transfer of the growth units within the bulk of the solution (Mullin,
 749 2001, Camacho et al., 2017). The effect of heat transfer on growth rate was also included by
 750 (Mersmann et al., 2002). Therefore both factors need to be considered when determining the growth
 751 mechanism and can be modelled using the followings (Mullin, 2001, Camacho et al., 2017):

$$752 \quad G_{power} = \frac{S - S_{crit}}{\frac{\rho_s}{k_{MT} C^* M_s} + \frac{1}{k_G (S - S_{crit})^{r-1}}} \quad (S.1)$$

$$753 \quad G_{B\&S} = \frac{S - S_{crit}}{\frac{\rho_s}{k_{MT} C^* M_s} + \frac{1}{k_G (S - S_{crit})^{-1/6} \exp(A_1 / (S - S_{crit}))}} \quad (S.2)$$

$$754 \quad G_{BCF} = \frac{S - S_{crit}}{\frac{\rho_s}{k_{MT} C^* M_s} + \frac{1}{k_G (S - S_{crit}) \tanh(A_2 / (S - S_{crit}))}} \quad (S.3)$$

755 Where G_{power} , $G_{B\&S}$ and G_{BCF} are the growth rates linking to the power law (Garside, 1985), B&S
 756 (Burton et al., 1951) and BCF (Burton et al., 1951) models; S is supersaturation defined by the ratio
 757 between the solute concentration at a solution temperature and the solubility at the same temperature;
 758 S_{crit} is a critical value of supersaturation; k_G is the growth rate constant; r is the growth exponent; A_1
 759 and A_2 are the thermodynamic parameters; ρ_s is the solute density; k_{MT} is the coefficient of mass
 760 transfer within the bulk of the solution; M_s is the solute molecular weight; C^* is the equilibrium
 761 concentration (solubility). The term $\frac{\rho_s}{k_{MT} C^* M_s}$ in Eqs. (S.1 – S.3) can be treated as a fitting parameter.
 762 In Eq. (S.1), if $r = 1$, it corresponds to a rough interface growth (RIG) mechanism (Weeks and Gilmer,
 763 1979).

764

765 S3. MPB Solution Method

766 Whilst the theoretical solution of the MPB equation can only be obtained for some ideal (simple)
767 cases, numerical solution methods can provide the most convenient and available approach. Lin et al.
768 (Lin et al., 2016) developed an invariant method of moments to obtain analytical solution of a PB
769 system, but this method could only be used for solving a one-dimensional homogeneous PB equation
770 with size independent growth rate. Therefore, many other different numerical solution methods have
771 been developed, for example, method of characteristics (Gunawan et al., 2004, Sotowa et al., 2000),
772 moment of classes (David et al., 1995, Puel et al., 2003a), high resolution discretisation schemes
773 (Gunawan et al., 2004, Ma et al., 2002, Wan et al., 2009), method of lines (Gerstlauer et al., 2001),
774 finite-element schemes (Gerstlauer et al., 2006), moving grid techniques (Kumar and Ramkrishna,
775 1997), hierarchical solution strategies based on multilevel discretisation (Pinto et al., 2007, Sun and
776 Immanuel, 2005), cell-ensemble method (Henson, 2005), Monte Carlo methods (Yu et al., 2015), etc.
777 In this study, a discretisation method (moment of classes) has been used to solve the MPB equation
778 (Eq. 1). In this, the three (x_1, x_2, x_3) size domains were discretised into i ($i = 1, N_1$), j ($j = 1, N_2$), k (k
779 $= 1, N_3$) classes, respectively, where N_1, N_2, N_3 are the total number of classes for the (x_1, x_2, x_3) size
780 domains and $\bar{x}_{1,i}(= x_{1,i} - x_{1,i-1}), \bar{x}_{2,j}(= x_{2,j} - x_{2,j-1}), \bar{x}_{3,k}(= x_{3,k} - x_{3,k-1})$ are the size of the $i, j,$
781 k classes for the (x_1, x_2, x_3). Hence a group of $N_1 \times N_2 \times N_3$ ordinary differential equations below can
782 be formulated and solved:

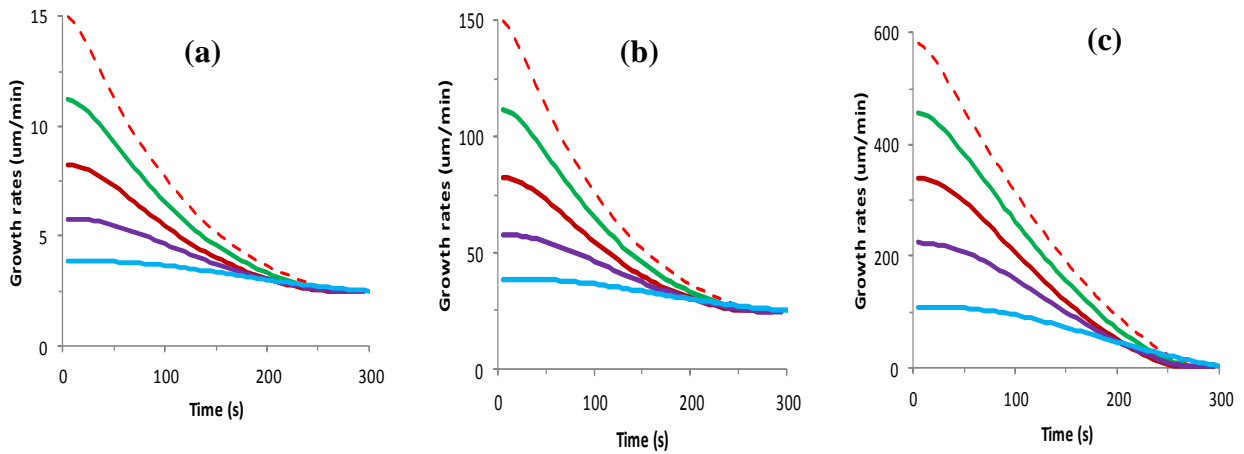
$$\begin{aligned}
783 \quad & \frac{1}{V_T(t)} \frac{d}{dt} \left[V_T(t) \int_{x_{1,i-1}}^{x_{1,i}} \int_{x_{2,j-1}}^{x_{2,j}} \int_{x_{3,k-1}}^{x_{3,k}} \Phi(x_1, x_2, x_3, t) dx_1 dx_2 dx_3 \right] + \\
784 \quad & G_1(\bar{x}_{1,i}, t) \left[\frac{x_{1,i+1} - x_{1,i}}{(x_{1,i} - x_{1,i-1})(x_{1,i+1} - x_{1,i-1})} \int_{x_{1,i-1}}^{x_{1,i}} \int_{x_{2,j-1}}^{x_{2,j}} \int_{x_{3,k-1}}^{x_{3,k}} \Phi(x_1, x_2, x_3, t) dx_1 dx_2 dx_3 + \right. \\
785 \quad & \left. \frac{x_{1,i} - x_{1,i-1}}{(x_{1,i+1} - x_{1,i})(x_{1,i+1} - x_{1,i-1})} \int_{x_{1,i}}^{x_{1,i+1}} \int_{x_{2,j-1}}^{x_{2,j}} \int_{x_{3,k-1}}^{x_{3,k}} \Phi(x_1, x_2, x_3, t) dx_1 dx_2 dx_3 \right] + \\
786 \quad & G_2(\bar{x}_{2,j}, t) \left[\frac{x_{2,j+1} - x_{2,j}}{(x_{2,j} - x_{2,j-1})(x_{2,j+1} - x_{2,j-1})} \int_{x_{1,i-1}}^{x_{1,i}} \int_{x_{2,j-1}}^{x_{2,j}} \int_{x_{3,k-1}}^{x_{3,k}} \Phi(x_1, x_2, x_3, t) dx_1 dx_2 dx_3 + \right. \\
787 \quad & \left. \frac{x_{2,j} - x_{2,j-1}}{(x_{2,j+1} - x_{2,j})(x_{2,j+1} - x_{2,j-1})} \int_{x_{1,i-1}}^{x_{1,i}} \int_{x_{2,j}}^{x_{2,j+1}} \int_{x_{3,k-1}}^{x_{3,k}} \Phi(x_1, x_2, x_3, t) dx_1 dx_2 dx_3 \right] + \\
788 \quad & G_3(\bar{x}_{3,k}, t) \left[\frac{x_{3,k+1} - x_{3,k}}{(x_{3,k} - x_{3,k-1})(x_{3,k+1} - x_{3,k-1})} \int_{x_{1,i-1}}^{x_{1,i}} \int_{x_{2,j-1}}^{x_{2,j}} \int_{x_{3,k-1}}^{x_{3,k}} \Phi(x_1, x_2, x_3, t) dx_1 dx_2 dx_3 + \right. \\
789 \quad & \left. \frac{x_{3,k} - x_{3,k-1}}{(x_{3,k+1} - x_{3,k})(x_{3,k+1} - x_{3,k-1})} \int_{x_{1,i-1}}^{x_{1,i}} \int_{x_{2,j-1}}^{x_{2,j}} \int_{x_{3,k}}^{x_{3,k+1}} \Phi(x_1, x_2, x_3, t) dx_1 dx_2 dx_3 \right] = 0 \quad (S.4)
\end{aligned}$$

790 The $N_1 \times N_2 \times N_3$ ordinary differential equations obtained, together with initial and boundary
791 conditions and also the equations for face-specific growth rates, and mass and heat balance in a batch
792 cooling crystalliser, form a complete set of the PB solution system. Further detail can be found in
793 literature (David et al., 1995, Ma et al., 2016, Ma and Wang, 2008, Ma et al., 2008, Puel et al., 2003a).

794

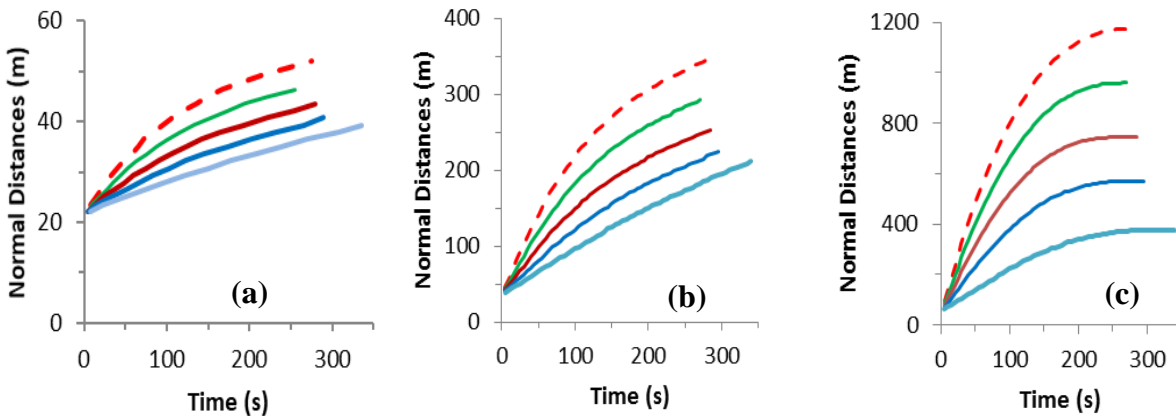
795 S4. Effect of Seeding Temperature

796



797

798 **Figure S.1** Evolution of faceted growth rates during crystallisation processes in face direction of (a)
799 face {101}, (b) face {10-1} and (c) face {011} under different seeding temperature (T_{seeds}) (or
800 supersaturations (S_{seeds})) ($T_{\text{seeds}} = 20.5^{\circ}\text{C}$ (or $S_{\text{seeds}} = 1.5$) – dashed red line; $T_{\text{seeds}} = 24.7^{\circ}\text{C}$ (or $S_{\text{seeds}} =$
801 1.4) – green line; $T_{\text{seeds}} = 28.9^{\circ}\text{C}$ (or $S_{\text{seeds}} = 1.3$) – red line; $T_{\text{seeds}} = 33.7^{\circ}\text{C}$ (or $S_{\text{seeds}} = 1.2$) – blue line;
802 $T_{\text{seeds}} = 39.0^{\circ}\text{C}$ (or $S_{\text{seeds}} = 1.1$) – light blue line).



803

804 **Figure S.2** Evolution of normal distances during crystallisation processes in face direction of (a) face
805 {101}, (b) face {10-1} and (c) face {011} under different seeding temperature (T_{seeds}) (or
806 supersaturations (S_{seeds})) ($T_{\text{seeds}} = 20.5^{\circ}\text{C}$ (or $S_{\text{seeds}} = 1.5$) – dashed red line; $T_{\text{seeds}} = 24.7^{\circ}\text{C}$ (or $S_{\text{seeds}} =$
807 1.4) – green line; $T_{\text{seeds}} = 28.9^{\circ}\text{C}$ (or $S_{\text{seeds}} = 1.3$) – red line; $T_{\text{seeds}} = 33.7^{\circ}\text{C}$ (or $S_{\text{seeds}} = 1.2$) – blue line;
808 $T_{\text{seeds}} = 39.0^{\circ}\text{C}$ (or $S_{\text{seeds}} = 1.1$) – light blue line).

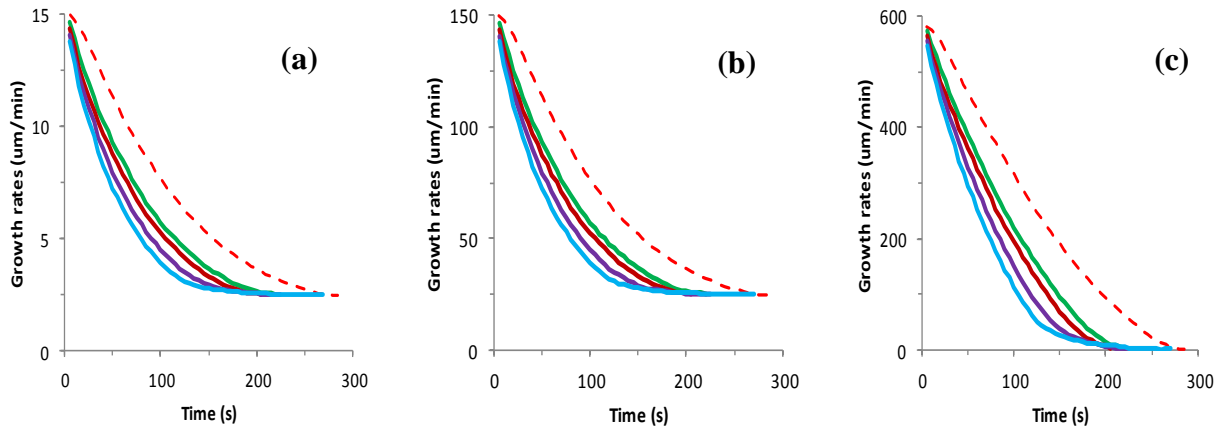
809

810

811

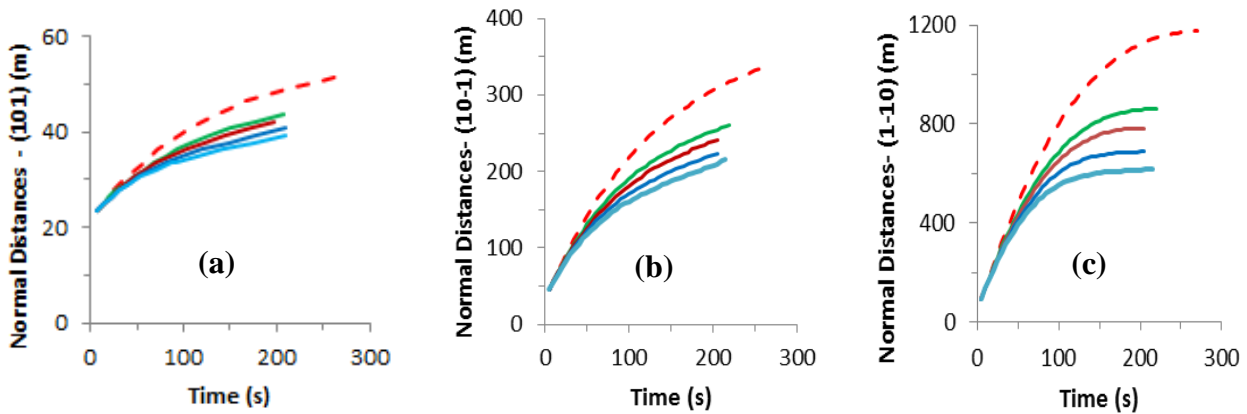
812 **S5. Effect of Seed Loading**

813



814

815 **Figure S.3** Evolution of faceted growth rates during crystallisation processes in face direction of (a)
 816 face {101}, (b) face {10-1} and (c) face {011} under different seed loading (X_{seeds}) ($X_{\text{seeds}} = 0.1\%$ –
 817 dashed red line; $X_{\text{seeds}} = 0.5\%$ – green line; $X_{\text{seeds}} = 1.0\%$ – red line; $X_{\text{seeds}} = 2.0\%$ – purple line; X_{seeds}
 818 = 5.0% – blue line).



819

820 **Figure S.4** Evolution of normal distances during crystallisation processes in face direction of (a) face
 821 {101}, (b) face {10-1} and (c) face {011} under different seed loading (X_{seeds}) ($X_{\text{seeds}} = 0.1\%$ – dashed
 822 red line; $X_{\text{seeds}} = 0.5\%$ – green line; $X_{\text{seeds}} = 1.0\%$ – red line; $X_{\text{seeds}} = 2.0\%$ – purple line; $X_{\text{seeds}} = 5.0\%$
 823 – blue line).

824

825

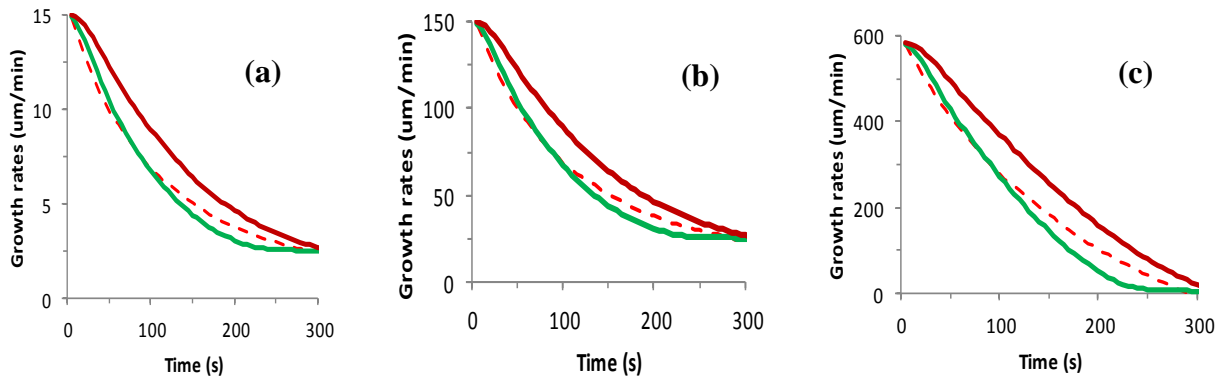
826

827

828

829 **S6. Effect of Seed Mean Shape**

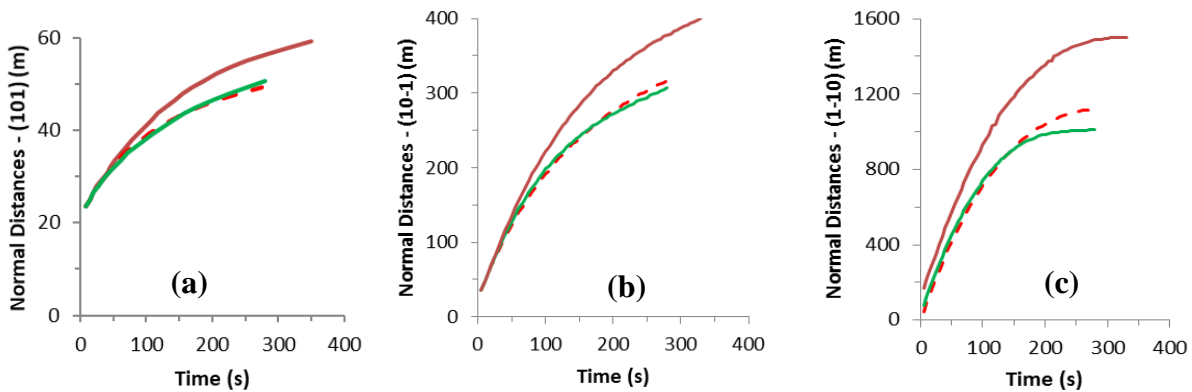
830



831

832 **Figure S.5** Evolution of faceted growth rates during crystallisation processes in face direction of (a)
 833 face {101}, (b) face {10-1} and (c) face {011} under different seed mean shape (M_{seeds}) with standard
 834 deviations of $\sigma_x, \sigma_y, \sigma_z = 8 \mu\text{m}$ ($M_{\text{seeds}} = (22, 27, 6 \mu\text{m})$ – dashed red line; $M_{\text{seeds}} = (22, 27, 40 \mu\text{m})$ –
 835 green line; $M_{\text{seeds}} = (22, 27, 131 \mu\text{m})$ – red line).

836



837

838 **Figure S.6** Evolution of normal distances during crystallisation processes in face direction of (a) face
 839 {101}, (b) face {10-1} and (c) face {011} under different seed mean shape (M_{seeds}) with standard
 840 deviations of $\sigma_x, \sigma_y, \sigma_z = 8 \mu\text{m}$ ($M_{\text{seeds}} = (22, 27, 6 \mu\text{m})$ – dashed red line; $M_{\text{seeds}} = (22, 27, 40 \mu\text{m})$ –
 841 green line; $M_{\text{seeds}} = (22, 27, 131 \mu\text{m})$ – red line).

842

843 **S7. References**

844 ALVAREZ, A. J. & MYERSON, A. S. 2010. Continuous plug flow crystallization of pharmaceutical
 845 compounds. *Crystal Growth & Design*, 10, 2219-2228.
 846 BORCHERT, C., RAMKRISHNA, D., NERE, N., VOIGT, A. & SUNDMACHER, K. 2009. On the
 847 prediction of crystal shape distributions in a steady-state continuous crystallizer *Chemical*
 848 *Engineering Science*, 64, 686-696.

849 BORCHERT, C. & SUNDMACHER, K. 2012. Efficient formulation of crystal shape evolution
850 equations. *Chemical Engineering Science*, 84, 85-99.

851 BRIESEN, H. 2009. Two-dimensional population balance modeling for shape dependent crystal
852 attrition. *Chemical Engineering Science*, 64, 661-672.

853 BURTON, W. K., CABRERA, N. & FRANK, F. C. 1951. The growth of crystals and the equilibrium
854 structure of their surfaces. *Philosophical Transactions of the Royal Society of London*, 243,
855 299-358.

856 CAILLET, A., SHEIBAT-OTHMAN, N. & FEVOTTE, G. 2007. Crystallization of monohydrate
857 citric acid. 2. modeling through population balance equations. *Crystal Growth & Design*, 7,
858 2088-2095.

859 CAMACHO, D. M., ROBERTS, K. J., MULLER, F., THOMAS, D., MORE, I. & LEWTAS, K.
860 2017. Morphology and Growth of Methyl Stearate as a Function of Crystallization
861 Environment. *Crystal Growth & Design*, 17, 563-575.

862 CHAKRABORTY, J., SINGH, M. R., RAMKRISHNA, D., BORCHERT, C. & SUNDMACHER,
863 K. 2010. Modeling of crystal morphology distributions. Towards crystals with preferred
864 asymmetry. *Chemical Engineering Science*, 65, 5676-5686.

865 DAVID, R., MARCHAL, P. & MARCANT, B. 1995. Modeling of Agglomeration in Industrial
866 Crystallization from Solution. *Chemical Engineering & Technology*, 18, 302-309.

867 FEVOTTE, G., ALEXANDRE, C. & NIDA, S. O. 2007. A Population Balance Model of the solution-
868 Mediated Phase Transition of citric acid. *AIChE Journal*, 53, 2578-2589.

869 GARSIDE, J. 1985. Industrial Crystallization from Solution. *Chemical Engineering Science*, 40, 3-
870 26.

871 GERSTLAUER, A., GAHN, C., ZHOU, H., RAULS, M. & SCHREIBER, M. 2006. Application of
872 population balances in the chemical industry - current status and future needs. *Chemical
873 Engineering Science*, 61, 205-217.

874 GERSTLAUER, A., MITROVIC, A., MOTZ, S. & GILLES, E. D. 2001. A population model for
875 crystallization processes using two independent particle properties. *Chemical Engineering
876 Science*, 56, 2553-2565.

877 GUNAWAN, R., FUSMAN, I. & BRAATZ, R. D. 2004. High resolution algorithms for
878 multidimensional population balance equations. *AIChE Journal*, 50, 2738-2749.

879 HENSON, M. A. 2005. Cell ensemble modeling of metabolic oscillations in continuous yeast
880 cultures. *Computers & Chemical Engineering*, 29, 645-661.

881 HOUNSLOW, M. J., LEWIS, A. E., SANDERS, S. J. & BONDY, R. 2005. Generic crystallizer
882 model: I. A model framework for a well-mixed compartment. *AIChE Journal*, 51, 2942-2955.

883 KUMAR, S. & RAMKRISHNA, D. 1997. On the solution of population balance equations by
884 discretization — III. Nucleation, growth and aggregation of particles. *Chemical Engineering
885 Science*, 52, 4659-4679.

886 KUVADIA, Z. B. & DOHERTY, M. F. 2013. Reformulating Multidimensional Population Balances
887 for Predicting Crystal Size and Shape. *AIChE Journal*, 59, 3468-3474.

888 KWON, J. S., NAYHOUSE, M., CHRISTOFIDES, P. D. & ORKOULAS, G. 2013. Modeling and
889 control of protein crystal shape and size in batch crystallization. *AIChE Journal*, 59, 2317-
890 2327.

891 KWON, J. S., NAYHOUSE, M., CHRISTOFIDES, P. D. & ORKOULAS, G. 2014. Modeling and
892 control of crystal shape in continuous protein crystallisation. *Chemical Engineering Science*,
893 107, 47-57.

894 LI, J., FREIREICH, B. J., WASSGREN, C. R. & LITSTER, J. D. 2013. Experimental validation of
895 a 2-D population balance model for spray coating processes. *Chemical Engineering Science*,
896 95, 360-365.

897 LIN, F., FLOOD, A. E. & MELESHKO, S. V. 2016. Exact solutions of population balance equation.
898 *Commun Nonlinear Sci Numer Simul*, 36, 378-390.

- 899 LIU, H. & LI, M. 2014. Two-compartmental population balance modeling of a pulsed spray fluidized
900 bed granulation based on computational fluid dynamics (CFD) analysis. *International Journal*
901 *of Pharmaceutics*, 475, 256-269.
- 902 LIU, J. J., HU, Y. D. & WANG, X. Z. 2013. Optimisation and control of crystal shape and size in
903 protein crystallisation process. *Computers and Chemical Engineering*, 57, 133-140.
- 904 LIU, J. J., MA, C. Y., HU, Y. D. & WANG, X. Z. 2010a. Effect of seed loading and cooling rate on
905 crystal size and shape distributions in protein crystallization—A study using morphological
906 population balance simulation. *Computers and Chemical Engineering*, 34, 1945-1952.
- 907 LIU, J. J., MA, C. Y., HU, Y. D. & WANG, X. Z. 2010b. Modelling protein crystallisation using
908 morphological population balance models. *Chemical Engineering Research & Design*, 88,
909 437-446.
- 910 LOVETTE, M. A., BROWNING, A. R., GRIFFIN, D. W., SIZEMORE, J. P., SNYDER, R. C. &
911 DOHERTY, M. F. 2008. *Crystal Shape Engineering*. *Industrial & Engineering Chemistry*
912 *Research*, 47, 9812-9833.
- 913 MA, C. Y., LIU, J. J. & WANG, X. Z. 2016. Measurement, modelling, and closed-loop control of
914 crystal shape distribution: Literature review and future perspectives. *Particuology*, 26, 1-18.
- 915 MA, C. Y. & ROBERTS, K. J. 2018. Combining Morphological Population Balances with Face-
916 Specific Growth Kinetics Data to Model and Predict the Crystallization Processes for
917 Ibuprofen. *Ind Chem Eng Res*, 57, 16379-16394.
- 918 MA, C. Y. & WANG, X. Z. 2008. Crystal growth rate dispersion modelling using morphological
919 population balance. *AIChE Journal*, 54, 2321-2334.
- 920 MA, C. Y. & WANG, X. Z. 2012. Model identification of crystal facet growth kinetics in
921 morphological population balance modeling of L-glutamic acid crystallization and
922 experimental validation. *Chemical Engineering Science*, 70, 22-30.
- 923 MA, C. Y., WANG, X. Z. & ROBERTS, K. J. 2007. Multi-dimensional population balance modelling
924 of the growth of rod-like L-glutamic acid crystals using growth rates estimated from in-
925 process imaging. *Advanced Powder Technology*, 18, 707-723.
- 926 MA, C. Y., WANG, X. Z. & ROBERTS, K. J. 2008. Morphological population balance for modelling
927 crystal growth in individual face directions. *AIChE Journal*, 54, 209-222.
- 928 MA, D. L., TAFTI, D. K. & BRAATZ, R. D. 2002. High-resolution simulation of multidimensional
929 crystal growth. *Industrial & Engineering Chemistry Research*, 41, 6217-6223.
- 930 MAJUMDER, A. & NAGY, Z. K. 2013. Prediction and control of crystal shape distribution in the
931 presence of crystal growth modifiers *Chemical Engineering Science*, 101 593-602.
- 932 MARCHAL, P., DAVID, R., KLEIN, J. P. & VILLERMAUX, J. 1988. *Crystallization and*
933 *precipitation engineering .1. An efficient method for solving population balance in*
934 *crystallization with agglomeration. Chemical Engineering Science*, 43, 59-67.
- 935 MENON, A. R., KRAMER, H. J. M., GRIEVINK, J. & JANSSENS, P. J. 2005. Modelling the cyclic
936 behaviour in a DTB crystallizer - a two-population balance model approach. *Journal of Crystal*
937 *Growth*, 275, e1373-e1381.
- 938 MERSMANN, A., BRAUN, B. & LOFFELMANN, M. 2002. Prediction of crystallisation
939 coefficients of the population balance. *Chemical Engineering Science*, 57, 4267-4275.
- 940 MULLIN, J. W. 2001. *Crystallization, USA*, Butterworth-Heinemann.
- 941 OULLION, M., PUEL, F., FEVOTTE, G., RIGHINI, S. & CARVIN, P. 2007. Industrial batch
942 crystallization of a plate-like organic product. In situ monitoring and 2D-CSD modelling: Part
943 1: Experimental study. *Chemical Engineering Science*, 62, 820-832.
- 944 PATIENCE, D. B., DELL'ORCO, P. C. & RAWLINGS, J. B. 2004. Optimal Operation of a Seeded
945 Pharmaceutical Crystallization with Growth-Dependent Dispersion. *Organic Process*
946 *Research & Development*, 8, 609-615.
- 947 PINTO, M. A., IMMANUEL, C. D. & DOYLE, F. J. 2007. A feasible solution technique for higher-
948 dimensional population balance models. *Computers & Chemical Engineering*, 31, 1242-1256.

949 PUEL, F., FEVOTTE, G. & KLEIN, J. P. 2003a. Simulation and analysis of industrial crystallization
950 processes through multidimensional population balance equations. Part 1: a resolution
951 algorithm based on the method of classes. *Chemical Engineering Science*, 58, 3715-3727.

952 PUEL, F., FEVOTTE, G. & KLEIN, J. P. 2003b. Simulation and analysis of industrial crystallization
953 processes through multidimensional population balance equations. Part 2: a study of semi-
954 batch crystallization. *Chemical Engineering Science*, 58, 3729-3740.

955 RAMKRISHNA, D. & MAHONEY, A. W. 2002. Population balance modeling. Promise for the
956 future. *Chemical Engineering Science*, 57, 595-606.

957 RAWLINGS, J. B., WITKOWSKI, W. R. & EATON, J. W. 1992. Modelling and control of
958 crystallizers. *Powder Technology*, 69, 3-9.

959 SATO, K., NAGAI, H., HASEGAWA, K., TOMORI, K., KRAMER, H. J. M. & JANSSENS, P. J.
960 2008. Two-dimensional population balance model with breakage of high aspect ratio crystals
961 for batch crystallization. *Chemical Engineering Science*, 63, 3271-3278.

962 SHI, D., EL-FARRA, N. H., LI, M., MHASKAR, P. & CHRISTOFIDES, P. D. 2006. Predictive
963 control of particle size distribution in particulate processes. *Chemical Engineering Science*,
964 61, 268-281.

965 SOTOWA, K. I., NAITO, K., KANO, M., HASEBE, S. & HASHIMOTO, I. 2000. Application of
966 the method of characteristics to crystallizer simulation and comparison with finite difference
967 for controller performance evaluation. *Journal of Process Control*, 10, 203-208.

968 SUN, N. F. & IMMANUEL, C. D. 2005. Efficient solution of population balance models employing
969 a hierarchical solution strategy based on a multi-level discretization. *Transactions of the*
970 *Institute of Measurement and Control*, 27, 347-366.

971 TEMMEL, E., EISENSCHMIDT, H., LORENZ, H., SUNDMACHER, K. & SEIDEL-
972 MORGENSTERN, A. 2016. A Short-Cut Method for the Quantification of Crystallization
973 Kinetics. 1. Method Development. *Crystal Growth & Design*, 16, 6743-6755.

974 ULBERT, Z. & LAKATOS, B. G. 2005. Modelling and simulation of crystallisers under non-perfect
975 micromixing conditions. *Chemical Engineering Science*, 60, 3525-3536.

976 VETTER, T., BURCHAM, C. L. & DOHERTY, M. F. 2014. Regions of attainable particle sizes in
977 continuous and batch crystallisation processes. *Chemical Engineering Science*, 106, 167-180.

978 WAN, J., WANG, X. Z. & MA, C. Y. 2009. Particle shape manipulation and optimization in cooling
979 crystallization involving multiple crystal morphological forms. *AIChE Journal*, 55, 2049-
980 2061.

981 WANG, X. Z. & MA, C. Y. 2009. Morphological population balance model in principal component
982 space. *AIChE Journal*, 55, 2370-2381.

983 WANG, X. Z., ROBERTS, K. J. & MA, C. Y. 2008. Crystal growth measurement using 2D and 3D
984 imaging and the perspectives for shape control. *Chemical Engineering Science*, 63, 1171-
985 1184.

986 WARD, J. D., MELLICHAMP, D. A. & DOHERTY, M. F. 2006. Choosing an operating policy for
987 seeded batch crystallization. *AIChE Journal*, 52, 2046-2054.

988 WARD, J. D., YU, C.-C. & DOHERTY, M. F. 2011. A New Framework and a Simpler Method for
989 the Development of Batch Crystallisation Recipes. *AIChE Journal*, 57, 606-617.

990 WEEKS, J. D. & GILMER, G. H. 1979. Dynamics of crystal growth. *Advances in Chemical Physics*,
991 40, 157-227.

992 YU, X., HOUNSLOW, M. J. & REYNOLDS, G. K. 2015. Monte Carlo solution of population
993 balance equations. *AIChE Journal*, 61, 2394-2402.

994 ZHANG, Y. C. & DOHERTY, M. F. 2004. Simultaneous prediction of crystal shape and size for
995 solution crystallization. *AIChE Journal*, 50, 2101-2112.